Towards Optical Excitation of Liquid-Dispersed Carbon Nanotubes inside Hollow-Core Photonic Bandgap Fiber

by

Anna Maria Houk

A thesis
presented to the University of Waterloo
in fulfillment of the
thesis requirement for the degree of
Master of Applied Science
in
Electrical and Computer Engineering - Quantum Information

Waterloo, Ontario, Canada, 2022

Author's Declaration

I hereby declare that I am the sole author of this thesis. This is a true copy of the thesis, including any required final revisions, as accepted by my examiners.

I understand that my thesis may be made electronically available to the public.

Abstract

This thesis is a study of the excitation of liquid-suspended carbon nanotubes (CNTs) confined in an optical waveguide. Desirable optical properties such as narrow emission and excitation bandwidths, as well as wide selectivity over the near-infrared spectrum, warrant the exploration of using CNTs as a gain medium in fiber-integrated lasers. Because of the necessity of liquid suspension to achieve high intensity fluorescence from CNTs, Hollow-core photonic bandgap fiber (HCPBF) was filled with common solvents, deionized water and deuterium dioxide(D_2O) to create an opto-fluidic waveguide. D_2O Liquid-HCPBFs with operational bandgaps in the near-infrared spectrum using telecom-wavelength HCPBFs drop to around half of their hollow-core transmission intensity due to propagating though a higher refractive index medium but still maintain a small mode-area. Preserving refractive-index scaling laws, the characteristics of hollow-core wavguides that make them desirable for engineering photon-particle interactions are maintained in the liquid-core counterparts. The interaction of the fiber mode with nano-scale suspended particles was first tested with indocyanine green, a fluorescent dye, due to its simple preparation and overlapping emission and excitation spectra with the bandgap of the liquid-HCPBFs. Within the Liquid-HCPBF, the fraction of fluorescence for ICG collected was an order of magnitude greater than that of collection efficiencies measured for dye samples contained in cuvettes. Following the results of the ICG dye, CNT solutions dominant with CNT chiralities within the Liquid-HCPBF bandgap were prepared and characterized. Initial Liquid-HCPBF with CNTs were began but the investigation with CNTs remains open.

Acknowledgements

I'd first like to thank the members of my thesis committee, Prof. Na Young Kim, Prof. Adam Wei Tsen, and Prof. Michal Bacjsy for their effort in reading and proving me with feedback on my thesis. I would also like to thank Prof. Kim for her role as my advisor and Prof. Bajcsy for his additional guidance and insights that helped me learn and progress on this work. I owe a great thanks to those who assisted in components of this project: HeeBong Yang for his help with the carbon nanotube samples, Yujia Yuan and Dr. Rubayet Al Maruf for their time and knowledge in the cleanroom and help fabricating the fiber splicing chips. Additionally, I am grateful to and Paul Anderson and Sai Sreesh Venuturumilli for their patience in teaching me essential lab skills. .

Dedication

To Lorenzo, for all your encouragement and support.

Table of Contents

List of Figures

List of Tables

Chapter 1

Introduction

Thanks to the latest developments in 1D and 2D materials, specialty optical waveguides, and fibers, it has become possible to design robust small-scale nonlinear devices and sensors[49, 58] that are not burdened by the need of constant realignment like traditional bulk-optical systems. Carbon Nanotubes (CNTs), a 1D material, possess unique optical properties that have found a variety of applications from mode-locking fiber integrated lasers[66, 67, 68, 69], biological and optical sensors[45, 46], and CNT-based single-photon sources[47]. Semiconducting-type CNTs can be optically excited and emit fluorescence[72] when well-dispersed in liquid solutions. With excitation, emission linewidths of only a few nanometers, and a wide selection over the near-infrared spectrum, CNTs are a promising candidate as fluorescent light source. Due to the need for liquid suspension for strong fluorescence from CNTs, integration into on-chip or fiber systems would require the development of a liquid waveguide. Such waveguides have been previously demonstrated, offering flexibility in tuning intensity and spectrum filtering through swapping the liquid medium for one of a different refractive-index[44]. Particle suspension in liquid waveguides has also been demonstrated for dielectric and fluorescent particles [43, 42] and could be used to develop on-chip and fiber-integrated sensors and fluorescent light sources.
To build a fiber-integrated device, we utilize Hollow-core photonic bandgap fibers (HCPBF). Such fibers are able to confine light to an air core and offer a low-loss, high threshold powers, and tight confinement that isn't feasible in conventional optical fibers. Because of the hollow core, it is possible to fill such fibers with gas or laser-cooled atoms and produce strong light-matter interactions[23, 24] and provide a tool for building single-photon interaction and nonlinear systems. Related work also suggests that the optical bandgap and strong interactions are preserved in liquid-filled HCPBF [19] despite lower refractive-index contrasts. Combining the ideas of particle suspension in liquid waveguide sensors with the

desirable mode-confinement of HCPBFs, this thesis explores the interaction of light with suspended fluorescent particles in liquid-filled HCPBFs to motivate the use of CNT optical properties in such devices.

The structure of this thesis is as follows: The optical properties of carbon nanotubes(CNTs) are introduced in Chapter 2, developing an argument for CNTs as a promising fluorescing nano-particle to be used in liquid-fiber applications. In Chapter 3 the theoretical background around fiber-optic waveguides using Total-Internal-Reflection (TIR) and Hollow-Core Photonic Crystal Fibers (HCPBF) is introduced. This is followed by the derivation of the bandgap-shift equation from the refractive-index scaling laws for HCPBF in low-index contrast regions, which provides the basis for predicting the bandgap of liquid-filled hollow-core fibers. Chapter 4 details the filling procedure for core-filled HCPBF, which transforms the HCPBF to guide light via TIR like a conventional optical fiber, and completely liquid-filled HCPBF, which should follow the scaling laws. Experimental confirmation of the predicted band-gap shift and transmission losses are done for H_2O and D_2O as filling materials. Chapter 5 introduces the optical properties of Indocyanine Green (ICG), a fluorescent dye used to study light-matter interactions between the particles suspended in the liquid-core and the mode of the fiber. Finally, Chapter 6 goes over the results of experiments with sorted CNTs suspended in H_2O and unsorted CNTs in D_2O, encountered challenges, and future considerations.

Chapter 2

Carbon Nanotubes

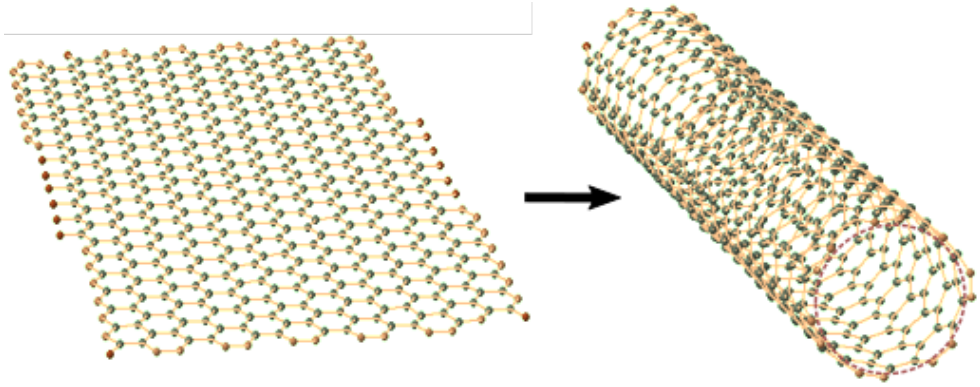

Figure 2.1: A sheet of graphene is rolled to form a (7, 5) chirality CNT. Graphene and CNT images were rendered using Dr. Shigeo Maruyama's "Nanotube Coordinate Generator" program [48].

First discovered by S.Iijima and T. Ichihashi in 1993, carbon nanotubes (CNTs) are single layers of graphene rolled up into a hollow cylinder near 1nm in diameter and average near 1μm in length. Due to the extreme diameter to length ratio, their geometry allows them to be treated as a 1D material. In this section follows a description of the attributes that make them attractive from an optical standpoint, going over their characterizing properties, nonlinear optical properties, and fluorescence.

2.1 Characterizing Carbon Nanotubes

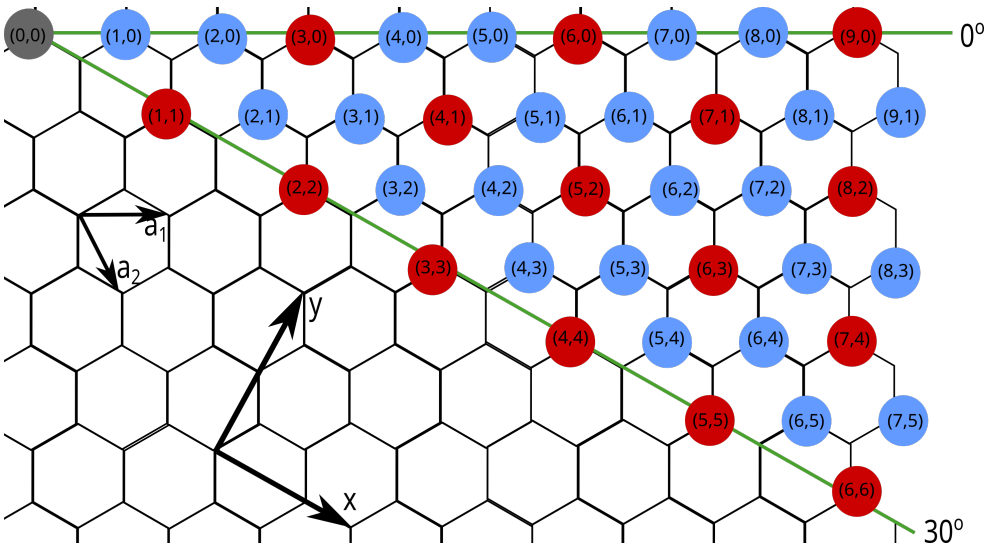

Figure 2.2: Chiralities of CNTs with red dots indicating metallic and blue dots semiconductors.

The main descriptive property of CNTs is the chiral vector, the inter-valued scaling of the unit vectors for the honeycomb structure of graphene, written in the form (n, m).

$$C_h = na_1 + ma_2 = (n, m) \tag{2.1}$$

The unit vectors describing the lattice are of equal length and in Cartesian coordinates are defined

$$a_1 = (\frac{\sqrt{3}}{2}, \frac{1}{2})\sqrt{3}a_{C-C} a_2 = (\frac{\sqrt{3}}{2}, -\frac{1}{2})\sqrt{3}a_{C-C} \tag{2.2}$$

where a_{C-C} is the length of the carbon bond. For graphene, a_{C-C}=1.421 (Å) but for CNTs is approximately 1.44(Å) with variation coming from the tube curvature[56]. From the chiral vector, much about the electronic and optical properties of individual CNTs can be inferred. The angle between the unit vectors, known as the chiral angle θ, gives the direction of the chiral vector and the diameter,d_t, of the CNT are related to the chiral numbers:

$$\theta = tan^{-1}\left[\frac{m\sqrt{3}}{m + 2n}\right] \tag{2.3}$$

$$d_t = \frac{a_{CC}\sqrt{3}}{\pi}\sqrt{n^2 + nm + m^2} \tag{2.4}$$

The chiral angle is typically defined between 0°(a "zigzag" configuration) and 30°(an "armchair" configuration), labeled in Fig.2.2 due to the six-fold rotational symmetry lattice, as CNTs of mirrored chiral angles will have the sample opto-electrical properties.
As can be seen from the above definition, the tube diameter of CNTs is quantized. This quantization stems from the additional electron confinement around their circumference

$$C_h \cdot \kappa = 2\pi q \tag{2.5}$$

as the cutting joining of the edges of graphene form the tubes only occurs at lines intersecting the lattice vertices. κ, the cutting line along the graphene energy bands, at integer value q positions forms a the corresponding pattern of metallic or a semiconductors [50] with all CNTs with a difference in chiral numbers $|m - n|$ that are multiples of 3 emerging as metallic. Work by H. Kataura et. al [55] first plotted the energy differences between the van Hoven transitions, corresponding to the peaks in the conduction and valence bands enumerated starting from the Fermi energy, indicated in the 1D DOS plots in Fig.2.3(b)(c) later determined from [56]. The relationship of the first van Hoven transition to the diameter is found to be

$$E_{11} = \frac{2\gamma a_{C-C}}{d} \tag{2.6}$$

is shown in Fig.2.3(a), with the average band gap energies split along semiconductor and metallic chiral values. The absorption peak wavelength of a nanotube sample is determined by the mean tube diameter, and the absorption spectral bandwidth will be determined by the tube diameter distribution of the CNT sample.

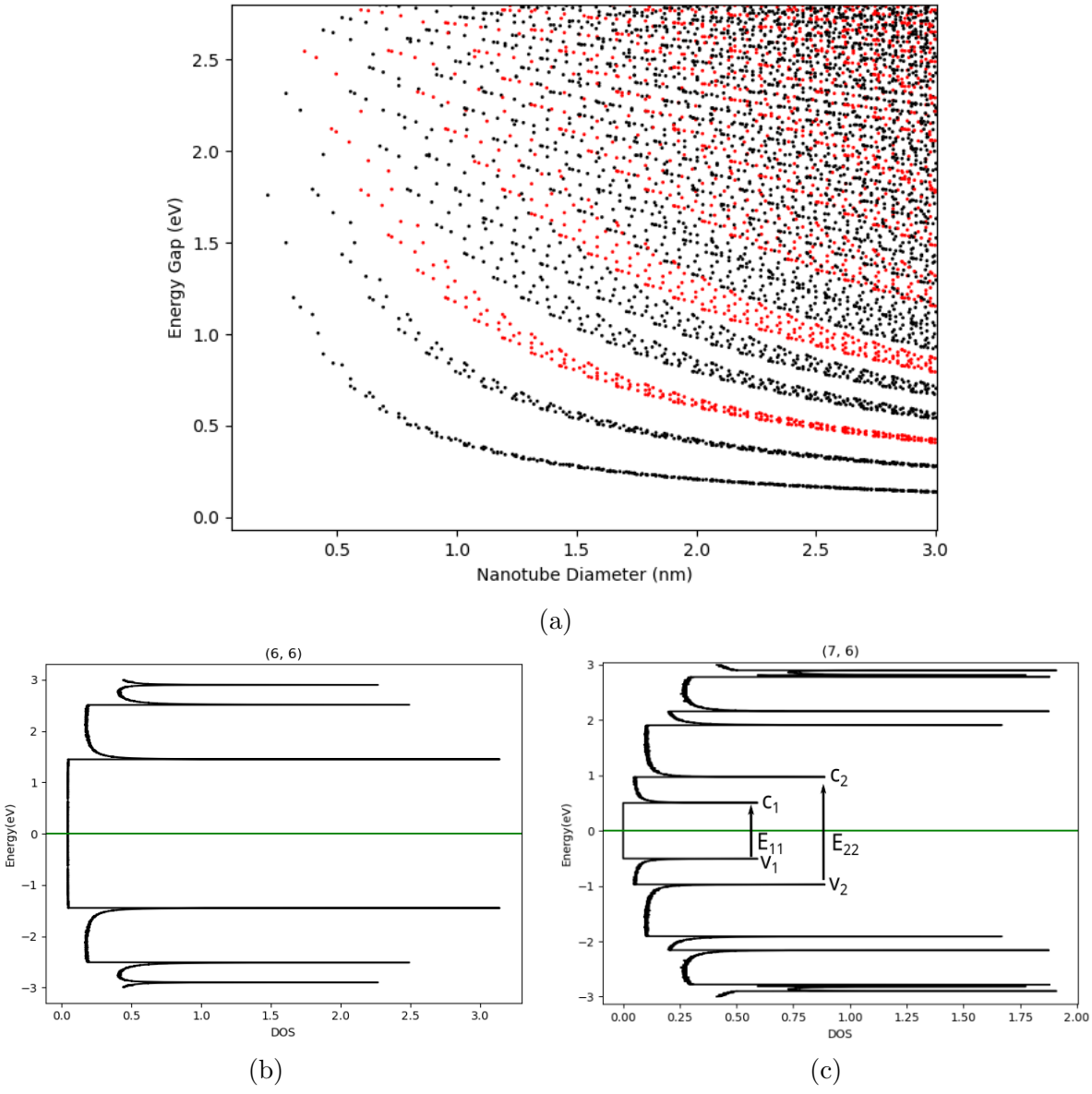

Figure 2.3: (a)The Kataura plot, showing the relationship between CNT diameter and energy separation. Red dots indicate metallic and black semiconducting. The density of states for (b) Metallic and (c) Semiconducting CNTs and their energy band gaps. The green line indicates the Fermi level. Plots generated using data from[57].

Polarization Dependence

Single isolated CNTs exhibit polarization dependence with the electric field in optical selection rules, i.e. the possible transitions from one quantum state to another [54]. Polarization dependence is only strong in zigzag-type nanotubes, the parity of the dipole operator (-1 in the horizontal plane dipole operator along the z-axis and +1the x-y plane) thus indicates absorption of light with the optical polarization parallel to the axial direction of the tube. However, in a bundle or random-oriented CNT grouping there will be no polarization dependence and it is not something that is of concern in CNTs dispersed in a solution.

2.2 Nonlinear Optical Properties of CNTs

The general relationship between the polarization and electric field of a material is defined [52] as

$$P(t) = \epsilon_0(\chi^{(1)}E(t) + \chi^{(2)}E^2(t) + \chi^{(3)}E^3(t) + ...) \tag{2.7}$$

where $\chi^{(1)}$ is the linear susceptibility and $\chi^{(2)}$ and $\chi^{(3)}$are the second and third order susceptibility. Due to symmetry of the CNT's structure, the second-order susceptibility is zero but a large third-order nonlinearity in CNTs has been measured [63] and is theorized to be a product of the one dimensional motion of the delocalized π-band electrons at a fixed lattice ion configuration [64]. The third-order nonlinearity is responsible for the saturable absorption α of a material as well as the nonlinear Kerr effect. The refractive index for such a material will be composed of the real part of the third-order susceptibility with I defining the optical intensity, n_0 as the linear refractive index, n_2 and is the nonlinear refractive index.

$$n = n_0 + n_2 I = n_0 + \frac{3Re[\chi^{(3)}]}{4\epsilon_0 c n_0^2} I \tag{2.8}$$

Saturable absorption is a phenomenon where high intensity light will reduce the absorption of a material, but at weak intensity, the light will be absorbed and cause attenuation. This property of materials with strong third-order susceptibility like CNTs can be used to filter out weaker optical signals in noisy optical pulses, while simultaneously allowing strong pulses to pass through. The absorption coefficient is composed of the imaginary part of the third-order susceptibility and α_0, α_{int}, and ω are the linear absorption coefficient, the

non saturable absorption coefficient, and optical angular frequency respectively:

$$\begin{aligned} \alpha &= \frac{\alpha_0}{1+\frac{I}{I_S}} + \alpha_{int} \\ &\sim \alpha_0 + \alpha_{int} + \frac{3\omega Im[\chi^3]}{2\epsilon_0 c^2 n_0^2} I \end{aligned} \tag{2.9}$$

the saturation intensity I_s is the power per unit area it takes in a steady state to reduce the absorption to half of completely saturated value, referred to as the unbleached state. Saturable absorption is observed in all materials with optical absorption resulting from electron transition between two energy levels [54], but it is rare to find materials that have a recovery time that has a fast recovery time compared to the pulse duration. In bundles of CNTs with a variety of diameter sizes, entanglement between semiconducting and metallic via electrons tunneling and coupling from semiconducting CNTs to metallic CNTs [59] can result in picosecond to femtosecond range recovery time. Bundled CNTs have found application in in ultra-fast laser applications where this sort of recovery time is needed, having been successful implemented in mode-locking femtosecond fiber-lasers[66, 67, 68, 69].

2.3 Fluorescence of CNTs

Arriving at the interest in CNTs for this thesis, semiconducting CNTs can be optically excited and emit fluorescence[72] when well-dispersed. Bundled CNTs have little fluorescence as interactions between CNTs cause increased quenching effects; where quenching is defined as any process that contributes to a decrease in fluorescence intensity. The highest fluorescence quantum yield measurements for CNTs have been achieved with CNTs suspended in aqueous solutions. Though certain solvents mix better with certain chiralities CNTs to increase fluorescence, isolation to single chiralities one of the largest factors in increasing fluorescence. Desired type of CNTs can be targeted and isolated in a single step using modified aqueous two-phase extraction(ATPS)[65].In this process, hydration modulating agents are mixed in to solutions to tune the arrangement of surfactants on their surface. Depending on the mixture, selected CNTs turn highly hydrophobic or hydrophilic, separating them from the rest of the mixture.
Fluorescence in carbon nanotubes is the product of absorption at the excitation frequency, corresponding to the second Van Hove optical transition (E22), labeled in Fig.2.3(c), from the valence to conduction bands, followed by relaxation to the first Van Hove optical transition (E11) from the conduction to valence band. The corresponding excitation and

emission wavelengths can be as a function of diameter in nanometers and chiral angle are degrees derived in [61]. The parameters fitted differ along CNT groups, having to do with chiral number differences: (n-m) mod 3 = 1 is group 1, (n-m) mod 3 = 2 is group 2, (n-m) mod 3 = 0 are metallic CNTs and do not fluoresce and so are excluded.
For group 1:

$$(Emission)\lambda_{11} = \left[\frac{10^7(cm^{-1})}{157.5 + 1066.9d_t} - A_{1m1}(cm^{-1})\frac{cos(3\theta)^{1.374}}{d_t^{2.272}}\right]^{-1} \tag{2.10}$$

$$(Excitation)\lambda_{22} = \left[\frac{10^7(cm^{-1})}{145.6 + 575.7d_t} + A_{2m1}(cm^{-1})\frac{cos(3\theta)^{0.828}}{d_t^{1.809}}\right]^{-1} \tag{2.11}$$

For group 2:

$$(Emission)\lambda_{11} = \left[\frac{10^7(cm^{-1})}{157.5 + 1066.9d_t} + A_{1m2}(cm^{-1})\frac{cos(3\theta)^{0.886}}{d_t^{2.129}}\right]^{-1} \tag{2.12}$$

$$(Excitation)\lambda_{22} = \left[\frac{10^7(cm^{-1})}{145.6 + 575.7d_t} - A_{2m2}(cm^{-1})\frac{cos(3\theta)^{1.110}}{d_t^{2.497}}\right]^{-1} \tag{2.13}$$

Additional parameters $A_{1m1}, A_{1m2}, A_{2m1}, A_{2m2}$, account for variations of spectrum in same diameter CNTs. Not all variation differences are yet explained but comparison of aqueous solutions[65][60] found spectral shifts of $\sim$2%.
Plots of the excitation-emission spectrum are using variational parameters from fitting to data of samples of individual SWNT in aqueous sodium dodecyl sulfate (SDS)[60] are shown in Fig.2.4. Group 1 CNTs have lower Stokes shifts, and small chiral angles ($< 2°$) while group 2 have higher Stokes shift and span full 0°to 30° chiral angle range with similar angles along chiral number difference $(n - m)$. Regardless of group, the in excitation and emission wavelengths increase with diameter.

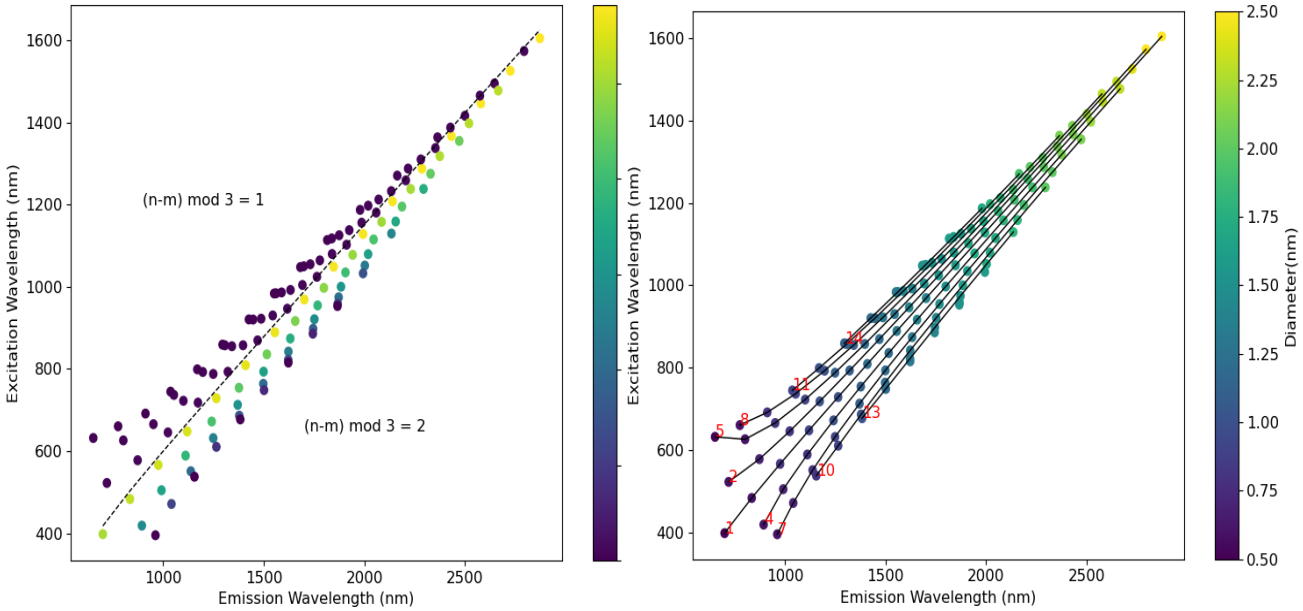

Figure 2.4: Group characteristics of CNTs colored by using variational parameters from[60], valid for diameters $> 0.5nm$. Color spectrum of plot denoting (a)chiral angle and (b)diameter. Increase in Stokes shifts with diameter along chiral difference $(n-m)$ lines, noted in red and connected by black lines.

Chapter 3

Hollow-Core Optical Waveguides

3.1 Conventional TIR Fibers

Conventional optical fibers (and optical waveguides in general) are guided by TIR. Structurally, this is composed of a high refractive-index core n_2 surrounded by a lower refractive-index cladding n_1, depicted in Fig.3.1. As light propagates through the the core, some light

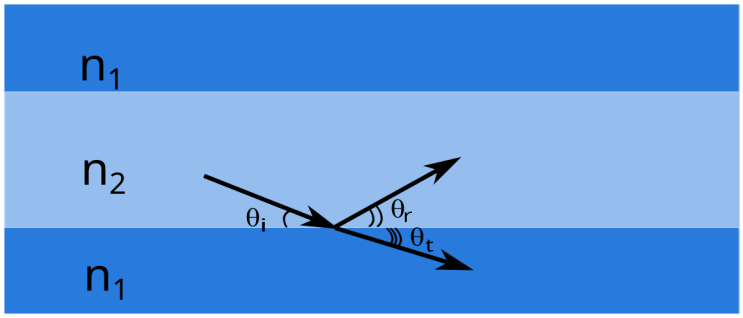

Figure 3.1: Light propagation through optical fiber. The incident θ_i, reflected θ_r, and transmitted θ_t rays at the core-cladding boundary

will be transmitted through the cladding while some is reflected back into the core. The relationship between the angles of incident and transmitted light is governed by Snell's Law:

$$n_1 cos(\theta_i) = n_2 cos(\theta_t) \tag{3.1}$$

If the refraction angle is at a minimum, then the light below a critical incident angle θ_c, will not propagate into the cladding and will only be reflected back into the core, hence "total

internal reflection". From Snell's law it is evident that the critical angle is dependent on the refractive-index contrast between the core and cladding,

$$\theta_c = arccos(n_2/n_1) \tag{3.2}$$

and that for TIR-guided fibers the core refractive index must be higher than that of the cladding otherwise light will just be transmitted through the cladding; this makes it physically impossible to make a TIR-based hollow-core fiber. The need for a higher core refractive index introduces limitations on the power transmission and intrinsic loss in TIR-guided fibers.

3.2 Hollow-Core Waveguides

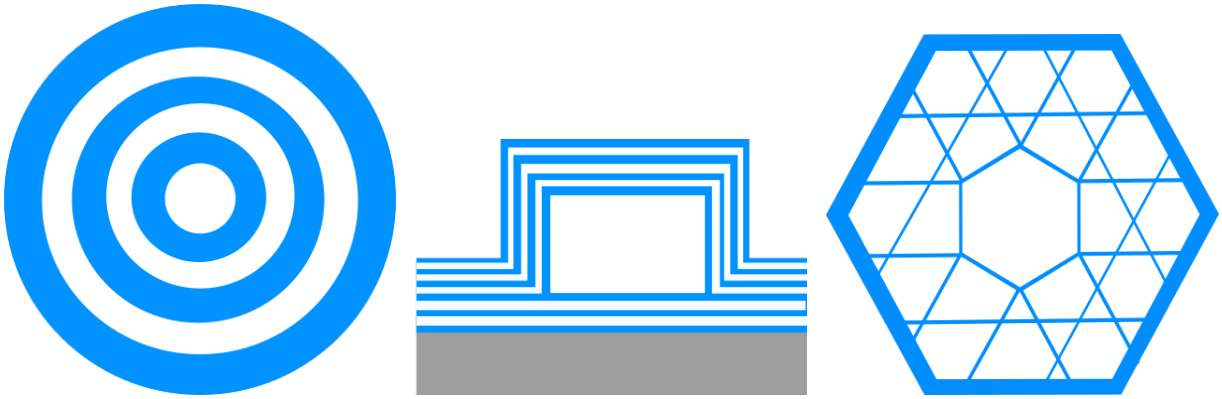

(a) (b) (c)

Figure 3.2: Cross-section of (a) Onion ring fiber (b) ARROW waveguide with multiple antiresonant layers (c) Kagome-lattice fiber.

TIR is not the only method of light confinement and guidance, and other methods of optical confinement have been able to achieve lower loss and higher intensities.
One of these methods is interference-based waveguides. The first 1D interference fiber, commonly referred to as "onion ring" fibers, was proposed in 1978 [1] and behaves as a Bragg grating perpendicular to the direction of propagation. The cross-section of this fiber is composed of concentric layers of alternating dielectric materials, with the number of layers to form a perfect bandgap being proportional to the bandgaps' width[2]. As light propagates, reflected and transmitted waves thought the layers of the cladding will destructively interfere allowing high reflection within the core.
Interference waveguides can be extended to 2D periodic structures, such as the hollow-core photonic bandgap fibers that are able to offer smaller mode areas than their 1D counterparts, or even without periodicity in ARROWs.
Antiresonant reflection optical waveguides (ARROWs) require a single dielectric layer at a thickness such that when light propagates from the low-index core to the higher-index ARROW layer, the phase shift Θ of the transverse wave meets the antiresonance condition $\Theta = m\pi$ (where m is an odd integer). This creates an antiresonant Fabry-Perot reflector in the transverse mode which allows propagation with low-loss over long distances; additional ARROW layers can also be added onto the waveguide in order improve efficiency. This type of waveguide was first demonstrated in 1986 as a solid-state waveguide[3] and used in semiconducting lasers with hollow-core designs following[4, 5].

Inhibited coupling (IC) fibers makeup another class of low-loss waveguides. In IC, waveguides carry a large phase mismatch between the modes guided through the core and the modes guided though through the cladding[6, 7], which take the form of a Kagome lattice. This mismatch prevents light in the core from leaking into the cladding.

Hollow-core waveguides have gained popularity in applications that require strong light-matter interaction, but aside from high light-confinement their low-index core design is a huge potential for integration with optofluidics[9]. When it comes to traditional TIR guided optical devices, the use of fluids for manipulation or as a material is hindered by the low refractive index of most liquids compared to the polymers and silica used. Already a feature of hollow-core waveguides, the design of liquid core ARROWs [10] and liquid filling of HCPBFs[19] promise on-chip or fiber-integrated optical manipulation and analysis of particles in liquids[11].

3.3 Photonic Crystal Bandgap

The refractive-index contrast constraints of traditional fibers are overcome by HCPBFs which are able to mitigate the propagation losses in the core by having a core of air, $n_{air} = 1$, the lowest possible refractive index. Light is instead trapped in the core by a photonic bandgap created by a surrounding photonic crystal cladding.

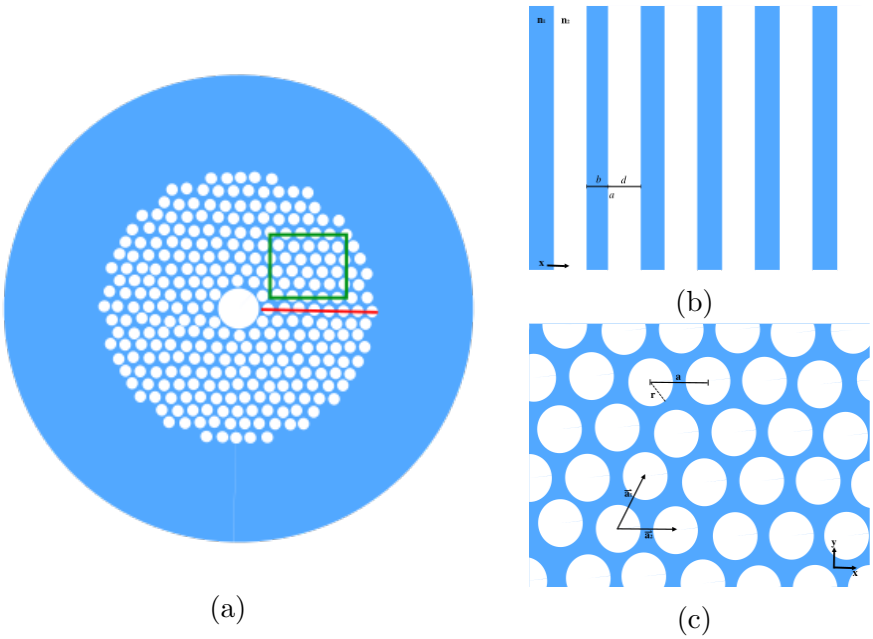

(a) (b) (c)

Figure 3.3: (a)Cross-section a honey-comb HCPBF highlighting the PC pattern (b) Reduction of PC to 1-dimension (c)The 2-dimensional PC.

Photonic crystals consist of alternating refractive index in periodic structure, such a the 1D stack depicted in Fig.3.3(b) or 2D periodic array of air-holes seen in the HCPBF cross-section in Fig.3.3(c) . A periodic non-magnetic medium will have repeating dielectric constant [12]

$$\varepsilon(\boldsymbol{r}) = \varepsilon(\boldsymbol{r} + \boldsymbol{a}) \tag{3.3}$$

Due to its discrete and invariant translational symmetry, the dielectric constant along the medium can be expanded as the Fourier series

$$\varepsilon(\boldsymbol{r}) = \sum_{\boldsymbol{G}} \varepsilon_{\boldsymbol{G}} e^{i\boldsymbol{G}\cdot\boldsymbol{r}} \tag{3.4}$$

where $\boldsymbol{G}$ are the reciprocal lattice vectors such that $\boldsymbol{G} \cdot \boldsymbol{a} = 2\pi n$. The electric field can also be expressed as the Fourier integral

$$\boldsymbol{E}(\boldsymbol{r}) = \iiint d^3\boldsymbol{k}\boldsymbol{A}(\boldsymbol{k}) e^{i\boldsymbol{k}\cdot\boldsymbol{r}} \tag{3.5}$$

Using the Maxwell equations (3.6) the wave equation can be written in terms of the electric field

$$\begin{cases} \vec{\nabla} \times \vec{H} &= -i\omega\epsilon(\vec{r})\vec{E} \\ \vec{\nabla} \times \vec{E} &= i\omega\mu_0\vec{H} \end{cases} \tag{3.6}$$

$$\boldsymbol{\nabla} \times (\boldsymbol{\nabla} \times \boldsymbol{E}) - \omega^2\varepsilon(\boldsymbol{r})\mu_0\boldsymbol{E} = 0 \tag{3.7}$$

Substituting (3.4) and (3.5) into the above equation results in the dispersion relation:

$$\boldsymbol{k} \times (\boldsymbol{k} \times \boldsymbol{A}(\boldsymbol{k})) + \omega^2\mu_0 \sum_{\boldsymbol{G}} \varepsilon_{\boldsymbol{G}} \boldsymbol{A}(\boldsymbol{k} - \boldsymbol{G}) = 0 \tag{3.8}$$

in where for any vector $\boldsymbol{K}$ the solutions of (3.8) for the coefficient $\boldsymbol{A}(\boldsymbol{K})$ are grouped with the coefficients $\boldsymbol{A}(\boldsymbol{K} - \boldsymbol{G})$, decoupling the coefficients of other vectors that cannot be expressed in the form $\boldsymbol{K} - \boldsymbol{G}$. Disregarding the decoupled vectors, the total electric field can be described as a superposition of normal modes with regard to a chosen vector $\boldsymbol{K}$:

$$\boldsymbol{E}_{\boldsymbol{k}}(\boldsymbol{r}) = \sum_{\boldsymbol{G}} \boldsymbol{A}(\boldsymbol{K} - \boldsymbol{G}) e^{i(\boldsymbol{k}-\boldsymbol{G})\cdot\boldsymbol{r}} \tag{3.9}$$

The Bloch theorem for the electric field can be pulled out from (3.9)

$$\boldsymbol{E}_{\boldsymbol{k}}(\boldsymbol{r} + \boldsymbol{a}) = e^{i\boldsymbol{k}\cdot\boldsymbol{a}} \boldsymbol{E}_{\boldsymbol{k}}(\boldsymbol{r}) \tag{3.10}$$

$$\boldsymbol{u_k}(\boldsymbol{r}) = \sum_{\boldsymbol{G}} \varepsilon_{\boldsymbol{G}} e^{i\boldsymbol{G}\cdot\boldsymbol{r}} \tag{3.11}$$

$$\varepsilon_{\boldsymbol{G}} = \frac{1}{V} \int d^3\boldsymbol{r} e^{-i\boldsymbol{G}\cdot\boldsymbol{r}} \boldsymbol{u_k}(\boldsymbol{r}) \tag{3.12}$$

Returning to (3.8), can fix ω to find the corresponding $\boldsymbol{K}$ and normal modes os the system. However, in the case of photonic crystals there are ranges of frequencies that have no $\boldsymbol{K}$s with real solutions, which implies that waves of these frequencies cannot propagate through the photonic crystal. These non-propagating frequencies are referred to as the photonic band gap.

3.3.1 1D Photonic Bandgap

1D photonic bandgap structure models for hollow-core optical fibers [14] demonstrate the core idea of bandgap fibers. In one dimension, the periodicity of dielectric constant is described by $\varepsilon(z) = \varepsilon(z + a)$ where $a = b + d$, the length of one period. The reciprocal lattice vector will be $\boldsymbol{G}_n = n\frac{2\pi}{a}\hat{z}$ and plugging into the Fourier series expansion of $\varepsilon(z)$ from (3.4)

$$\varepsilon(z) = \sum_{n=-\infty}^{\infty} \varepsilon_n e^{in\frac{2\pi}{a}\hat{z}} \tag{3.13}$$

From the reduction to propagation in the z-direction with the electric field oriented in x-direction, (3.8) simplifies to

$$K^2 A(K) + \omega^2 \mu_0 \sum_{n=-i\infty}^{\infty} \varepsilon_n A(K - n\frac{2\pi}{a}) = 0 \tag{3.14}$$

Expanding the Fourier coefficients to the 1st order and reducing the equations to the dominant coefficients of the form $A(K)$ and $A(K - \frac{2\pi}{a})$. $|K - g| = K$ and $K = \frac{\pi}{a}$ gives a system of equations that can be solved to find the dispersion relation $\omega(K)$.

$$\begin{cases} \big(K^2 - \omega^2\mu_0\varepsilon_{00}\big)A(K) = \omega^2\mu_0\varepsilon_1 A(K - g) \\ \omega^2\mu_0\varepsilon_{-1}A(K) = \big((K - g)^2 - \omega^2\mu_0\varepsilon_{00}\big)A(K - g) \end{cases} \tag{3.15}$$

The equations relating these two modes have a solution at

$$\big(K^2 - \omega^2\mu_0\varepsilon_{00}\big)\big((K - g)^2 - \omega^2\mu_0\varepsilon_{00}\big) - \big(\omega^2\mu_0\varepsilon_1\big)\big(\omega^2\mu_0\varepsilon_{-1}\big) = 0 \tag{3.16}$$

Noting that $\varepsilon_1 = \varepsilon^*_{-1}$ and $K \approx 2g$ simplifies the relationship to

$$\omega^2_{\pm} = \frac{K^2}{\mu_0(\varepsilon_{00} \mp |\varepsilon_1|)} \tag{3.17}$$

The dispersion relation has two possible solutions, which specify the top and bottom of the photonic bandgap edges, as illustrated in Fig.3.4.

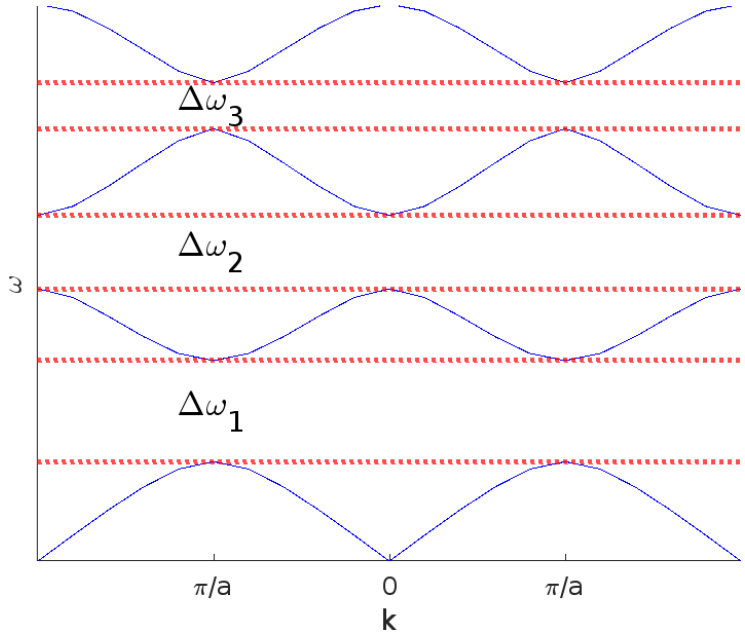

Figure 3.4: Band plot for a 1D photonic crystal with parameters-,-, solved using Finite Difference Time Domain(FDTD) method[17].

If solving for the wavevector at a frequency between the two roots $\omega_{\pm}$, only complex solutions will exist. This means that only evanescent waves, not electromagnetic waves, propagate through the medium while the electromagnetic waves are reflected back; the medium acts as a mirror for the bandgap wavelengths.
This is the phenomenon that allows for HCPBF to guide certain frequencies of light: wavelengths in the bandgap are reflected by surrounding Bragg Grating confining them to the core of the fiber, while the rest are allowed to propagate through the grating.

3.3.2 2D Photonic Bandgap

To understand the full picture of light propagation in hollow-core fiber, the expansion to the 2D case pictured in Fig.3.3c is needed. However, with the electromagnetic waves now propagating in two dimension there is an added layer of complexity with the TE TM wave polarizations and the bandgaps. In addition to controlling the refractive index of the material and the period of the lattice, the lattice structure and hole radius will affect the performance of the photonic crystal, the latter playing a large role in the completeness of the photonic bandgap. In the 2D photonic crystal, the in-plane guided modes will have either magnetic fields in-plane and electric fields perpendicular to the lattice (TE modes), or electric fields in-plane and magnetic fields perpendicular to the lattice (TM modes). As the TE and TM modes are perpendicular to each other they may exhibit wildly different dispersion relations, which means that an optical bandgap is not guaranteed to persist for all polarizations[13]. This is certainly the case for square lattice phonic crystals, but other patterns such as the honeycomb (which is the structure in our HCPBF) have a bandgap persisting for all polarizations[15]. It is important to consider all polarization effects when making decisions about photonic crystal patterns for two or more dimensions.

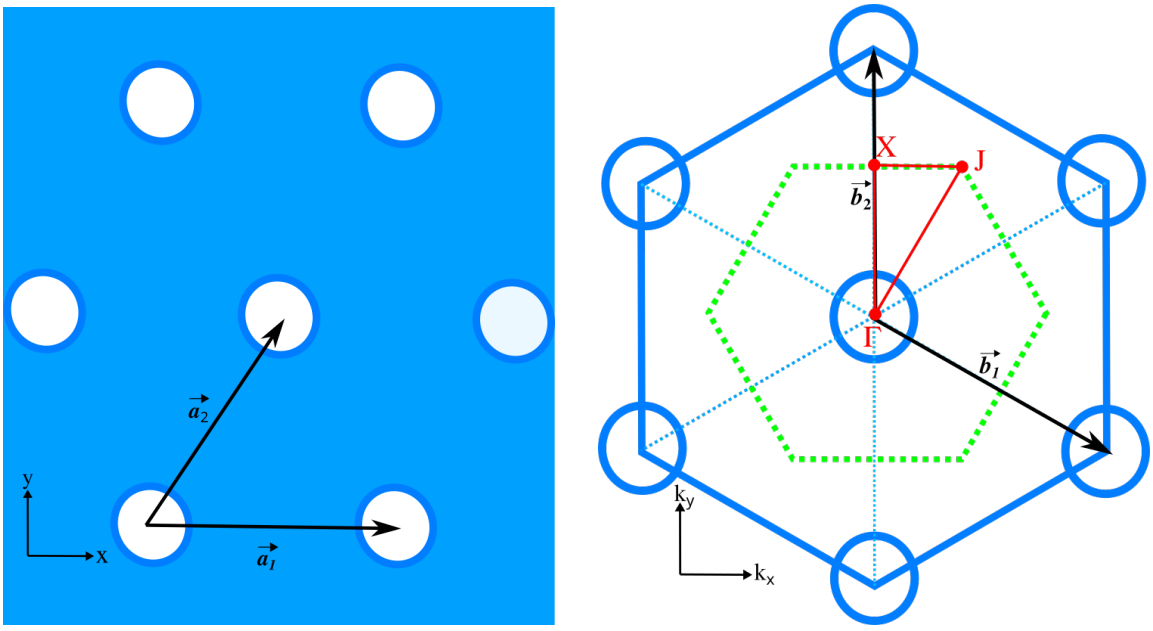

(a) (b)

Figure 3.5: (a) primitive lattice vectors and (b) primitive reciprocal lattice vectors with first Brillouin zone (green) and irreducible Brillouin zone (red) depicted for a honeycomb lattice structure.

Considering the lattice structure in Fig.3.5(a) and taking propagation in the xy-plane ($K_z = 0$ and $z = 0$ for simplicity), the wavevector and position vectors reduce to $\boldsymbol{K}_{||} = k_x\hat{x} + k_y\hat{y}$ and $\boldsymbol{r}_{||} = x\hat{x} + y\hat{y}$. The primitive lattice vectors of a honeycomb photonic crystal will be:

$$\boldsymbol{a}_1 = a\hat{x} \qquad \boldsymbol{a}_2 = \frac{a}{2}\hat{x} + \frac{a\sqrt{3}}{2}\hat{y} \tag{3.18}$$

and transforming to the momentum-space, $\boldsymbol{b}\cdot\boldsymbol{a} = 2\pi\delta_{ij}$, as shown in Fig.3.5(b) the primitive reciprocal lattice vectors are

$$\boldsymbol{b}_1 = \frac{2\pi}{a}\hat{x} - \frac{2\pi}{a\sqrt{3}}\hat{y} \qquad \boldsymbol{b}_2 = \frac{4\pi}{a\sqrt{3}}\hat{y} \tag{3.19}$$

Taking these in combination of n, m integer scaling factors, the reciprocal lattice vector is defined $\boldsymbol{G}_{||} = n\boldsymbol{b}_1 + m\boldsymbol{b}_2$. The electromagnetic field defined for a two dimensional system is

$$\boldsymbol{E}(\boldsymbol{r}) = e^{i\boldsymbol{k}\cdot\boldsymbol{r}} \sum_{m=-\infty}^{\infty} \sum_{n=-\infty}^{\infty} \boldsymbol{E}_{m,n} e^{i(n\boldsymbol{b_1} + m\boldsymbol{b_2})\cdot\boldsymbol{r}} \tag{3.20}$$

and the correlating Fourier expansion of dielectric function (3.12)

$$\varepsilon_{\boldsymbol{G}_{||}} = \frac{1}{a' \cdot b'} \int dxdy e^{i(G_x x + G_y y)} \boldsymbol{u}_{\boldsymbol{k}}(x, y) \tag{3.21}$$

are substituted into (3.6). By utilizing the lattice symmetry and periodicity, the problem can be restricted to only solve for Bloch modes inside the of the irreducible Brillouin zone. The first Brillouin zone is defined by the perpendicular bisectors to the primitive reciprocal lattice vectors, depicted in green in Fig.3.5(b) and can be further subdivided into the irreducible Brillouin zone shown in red. In order to find the photonic bandgap, solving the dispersion equation just along the irreducible Brillouin zone is sufficient. For a honeycomb lattice, the k-path to follow would be

$$\begin{cases} |\Gamma X| = \frac{2\pi}{a\sqrt{3}}, & k_x = 0, 0 < k_y < \frac{2\pi}{\sqrt{3}a} \\ |XJ| = \frac{2\pi}{3a}, & 0 < k_x < \frac{2\pi}{3a}, k_y = \frac{2\pi}{\sqrt{3}a} \\ |\Gamma J| = \frac{4\pi}{3a}, & 0 < k_x < \frac{2\pi}{3a}, k_y = \sqrt{3}k_x \end{cases} \tag{3.22}$$

Discretizing (3.20) and (3.21) then picking a few points along the k-path, numerical methods can be used to solve for the optical bandgap. Fig.3.6 shows the resulting TE bandgap for a honeycomb lattice with parameters $\varepsilon = 11, \frac{r}{a} = 0.34$, $a = 3.8\mu$m using Plane Wave Expansion(PWE)[17].

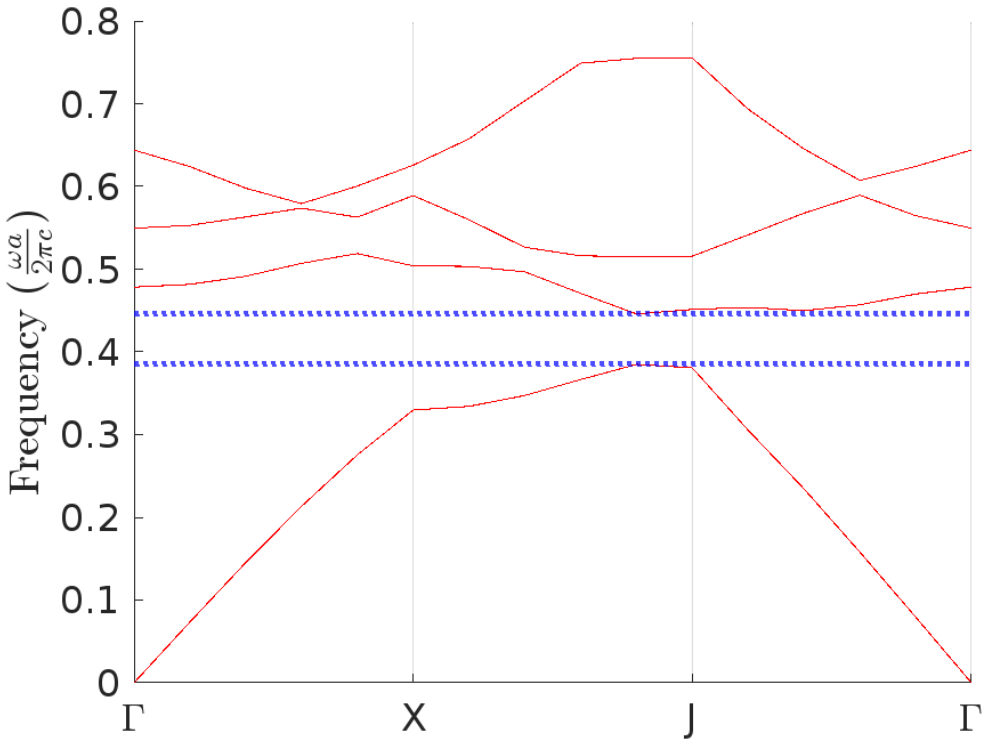

Figure 3.6: Band plot along the irreducible Brillouin zone for a honeycomb lattice with parameters $\varepsilon = 11, \frac{r}{a} = 0.34$, $a = 3.8\mu$m. Solved by using the Plane Wave Expansion(PWE) numerical method.

3.3.3 Bandgap Shift

The position of the HCPBF bandgap is dependent on the periodicity refractive-index and changing the material within the photonic crystal will cause a change in the bandgap. Though a small index contrast in the a periodic medium is assumed in the derivation, the bandgap shift has been experimentally confirmed to still hold under high contrasts[19]. The scalar wave equation for a given periodic medium will maintain the same bandgap structure but scaling the wavelength proportionately in compensation[18]. The scaling law for the wave equation for the transverse coordinates $X = x\Lambda^{-1}$ $Y = y\Lambda^{-1}$ where Λ is a solution to the transverse scale.

$$n(X,Y) = \begin{cases} 1, & n_1 \text{ (high RI)} \\ 0, & n_2 \text{ (low RI)} \end{cases} \tag{3.23}$$

and factors into the normalized scaled wave equation:

$$\nabla_\perp^2 \Psi + (v^2 n(X,Y) - w^2)\Psi = 0 \tag{3.24}$$

With $\nabla_\perp = \partial^2/\partial X^2 + \partial^2/\partial Y^2$ solving for the frequency parameter v^2 and eigenvalue w^2:

$$\begin{aligned} v^2 &= \Lambda^2 k^2 (n_1^2 - n_2^2) \\ w^2 &= \Lambda^2 (\beta^2 - k^2 n_2^2) \end{aligned} \tag{3.25}$$

From the equation above it is evident that the eigenvalue is determined by the frequency parameter and the index distribution function $n(X,Y)$. This implies that w^2 and v^2 are invariant with changes to the parameters $k = \omega/c, \Lambda, n_1, n_2$. In the HCPBF case where the glass refractive index is held constant and the air in the fiber is replaced by a new material. The equations can be rewritten with $n_1 = n_{glass}$ and $n_2 = n_{air} = 1$:

$$\begin{aligned} v^2 - w^2 &= \Lambda^2 (k^2 n_{glass} - \beta^2) \\ v &= k\Lambda n_{glass} \sqrt{n_{air} - \frac{n_{air}}{n_{new}}} \end{aligned} \tag{3.26}$$

The initial index contrast $N_0 = \frac{n_{air}}{n_{glass}}$ moves to $N = \frac{n_{new}}{n_{glass}}$ with the change in RI $n_{air} < n_{new} < n_{glass}$. This leads to the new center bandgap to be governed by the equation:

$$\lambda = \lambda_0 \sqrt{\frac{1 - N^{-2}}{1 - N_0^{-2}}} \tag{3.27}$$

3.4 Particle-Mode Interaction and Optical Depth

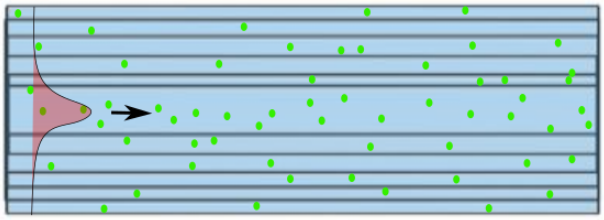

Figure 3.7: Diagram of a Gaussian mode traveling through a fully-filled HCPBF with normally suspended nanoparticles.

Optical depth (OD) is a measurement of the opacity of a system, related to the transmitted intensity by $T = exp(-OD)$. With particles distributed throughout the fiber, the interaction between the beam and particles inside the fiber needs to be taken into account. When considering a single particle interacting with the mode function of a waveguide the strength of the particle interaction will depend on its position within the mode[25, 26]. The effective mode area of the waveguide is then relevant only in relation to the position of the particle.

$$\sigma_M = \frac{\int dxdy|f_k(x,y)|^2}{|f_k(x_p,y_p)|^2} \tag{3.28}$$

where $f_k(x,y)$ is the transverse mode function and $f(x_p,y_p)$ is the position of the particle. In the case of a Gaussian mode function (as would be in a HCPBF), the photon interaction with the particle will be stronger in the center of the mode and weak at the edges. The optical depth (OD) for a single particle the ratio of the scattering cross-section to that of the effective mode-area $OD = \frac{\sigma_0}{\sigma_M}$, so to find the optical depth over the entire ensemble the product of the number density of the sample and optical depth of each emitter is integrated over the volume :

$$OD_{fiber} = \int_0^{L'} \int_0^{r'} n(r,z)OD(2\pi r)drdz \tag{3.29}$$

where r' and L' represent the radius and length of the ensemble. When the fibers are fully liquid cladding and core, due to the low interaction and guidance of photons in the PC structure, an approximation is made constricting the mode function strictly to the core. This simplifies the dimensions of the integration to just be the radius and length of the fiber. This assumes that the particulates outside of the core do not have a significant contribution. If the distribution of molecules is taken to be uniform along the fiber length

and radius of the core, then the number density is:

$$n(r,z) = \frac{N_{particle}}{V_{fiber}} = \frac{N_{particle}}{\pi r_{core}^2 L_{fiber}} \tag{3.30}$$

The integral will simplify to

$$\begin{aligned} OD_{fiber} &= \int_0^{L_{fiber}} \int_0^{r_{core}} n(r_{core}, L_{fiber}) \sigma_0 \frac{2}{\pi w_0^2} e^{-\frac{2r^2}{w_0^2}} (2\pi r) dr dz \\ &= N_{particle} \frac{\sigma_0}{\pi r_{core}^2} \left(1 - e^{\frac{-2r_{core}^2}{w_0^2}}\right) \end{aligned} \tag{3.31}$$

Chapter 4

Liquid-Filled HCPBF

In this chapter follows a background on different filling methods, the integrity of the scaling laws, and transmission of liquid-filled HCPBF.

4.1 Experimental Set-Up

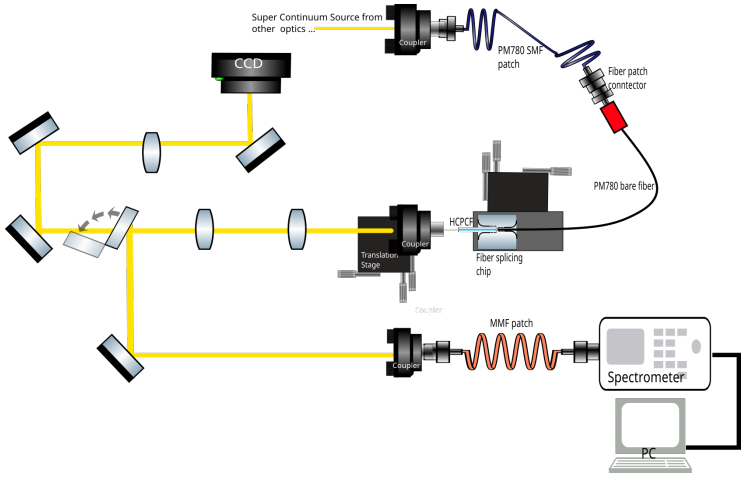

Figure 4.1: Fiber transmission experimental set-up. The path to the CCD camera is used to monitor the modeshape coming out of the fiber and the path to the spectrometer is used to measure the transmission spectrum of the fiber.

For the transmission measurements, shown in Fig.4.1, fibers were cut to be between 6cm and 8cm in length. To ensure consistent coupling and positioning, light was coupled to the core of the fiber by connecting to a solid-core PM780HP fiber via a mechanical splicing chip [20].
In our experiments two different filling methods are tested: full fiber filling, and selective filling, as well as two filling liquids: deionized water (which will be referred to as DI Water or H_2O) and heavy water D_2O. Fibers that are fully-filled with water will produce a

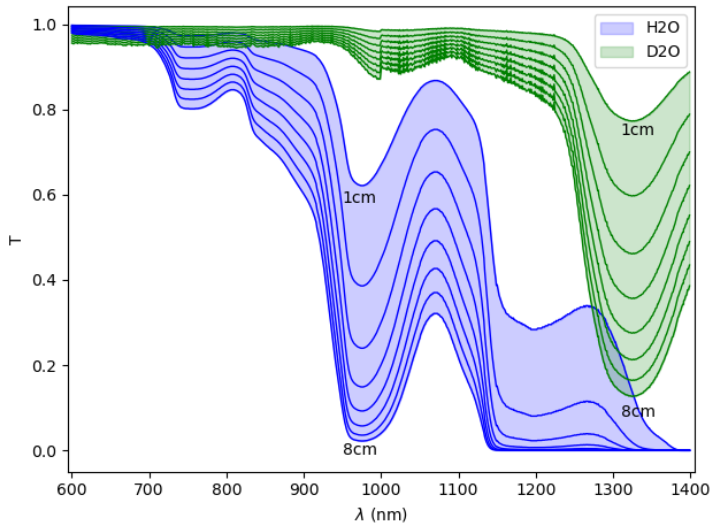

Figure 4.2: The transmission of heavy water(green) and regular water(blue) is shown for slabs of thickness ranging from 1cm to 8cm in increments of 1cm using absorption data by [22].

frequency shift in the bandgap. On the other hand, when the core is selectively filled with water, the core refractive index will be greater than effective refractive index of the cladding and light will be guided via total-internal reflection. H_2O, while widely available and a common solvent, has high absorption loss in the near infrared (NIR) but its most common isotope D_2O has comparatively much less absorption loss in the same region (Fig.4.2). The transmission in HCPBF are explored for H_2O for its ubiquity while D_2O for its suitability as a filling liquid in the NIR.

4.1.1 HCPBF Specifications

Photonic bandgap fibers HC-1500 and HC-800B were purchased from Thor Labs but manufactured by NKT Photonics. HC-1500 fiber is designed with a central wavelength of 1550nm. The cladding diameter of the fiber is 120±2μm and has a core diameter of 10±1μm with a surrounding photonic crystal structure of 70±5μm in diameter, guiding light with a Gaussian modeshape of 9±1μm beam waist. Less than 5% of optical power propagates through the silica material of the fiber and attenuation within the operating wavelengths (1490nm - 1680nm) is under 30 dB/km[39]. HC-800B fiber is designed with a central wavelength of 800nm. The cladding diameter of the fiber is 130±5μm and has a core diameter of 7.5±1μm with a surrounding photonic crystal structure of 45±5μm in diameter, guiding light with a Gaussian modeshape of 5.5±1μm beam waist. Attenuation within the operating wavelengths (770nm - 870nm) is under 250 dB/km[40].

4.1.2 On-chip Mechanical Splicing

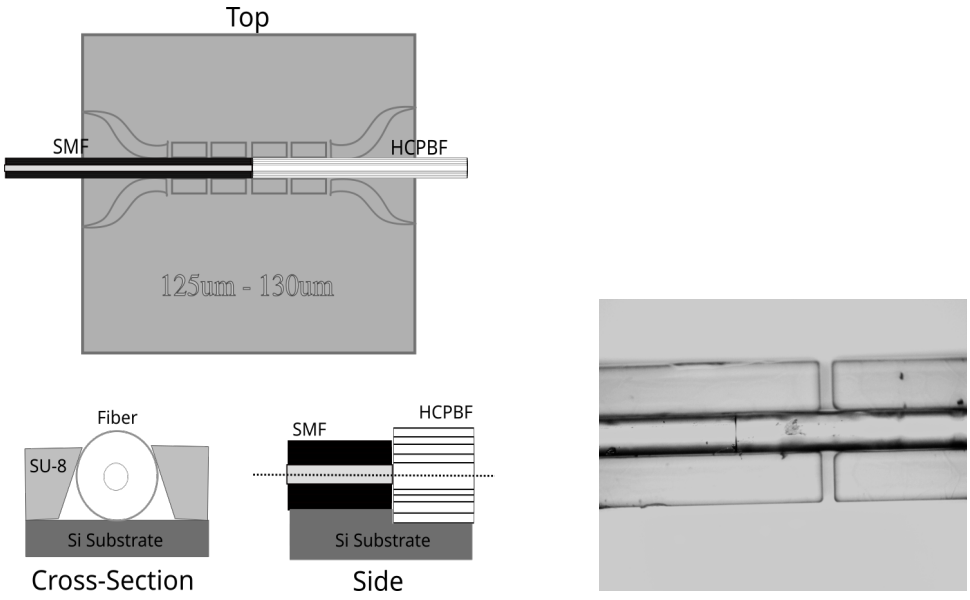

(a) (b)

Figure 4.3: (a) Top, side, and cross-section illustrations of a mechanical splicer chip to align a 125μm diameter to a 130μm diameter fiber. (b) A top-view optical microscope image of coupled fibers in a mechanical slicing chip.

In order to perform measurements, light needed to be coupled into the HCPBF consistently and with high efficiency. However, if the HCPBF were to be spliced to a SMF (single-mode fiber) as is traditionally done with a fusion splicer, the lattice structure of the photonic crystal will melt and distort, resulting in significant losses in coupling. In order to reduce the losses of fusion splicing HCPBF, the fibers were instead coupled via mechanical splicing.

With mechanical splicing, the fiber faces are butt-coupled and held in-place with a mechanical structure. Such a opto-mechanical splicing chip had already been developed by NPQO lab member Dr. Rubayet Al Maruf [20]. An illustration of the chip design is shown in 4.3(a), showing that the horizontal movement of fibers placed in the chip is constrained by a clamp micro-structure with undercut walls in order to prevent vertical movement of the fiber. In order to align different diameter fiber (such as a SMF to a HCPBF) one side of the chip's the silicon substrate is etched to create a step so that the fiber cores are aligned on the same optical axis.

The [20] chips provide a high-efficiency fiber-integrated coupling method. Between SMF and HCPBF, coupling efficiencies between 75%- 80% are consistently measured, something not easily achieved with fusion splicing or free-space coupling methods.

4.2 Selective Filling

Filling Method

To selectively fill the core of 800nm HCPBF, the photonic crystal cladding was collapsed while leaving the hollow-core open and is similarly filled with liquid using capillary action. The cladding is collapsed by placing the HCPBF opposite of a solid-core fiber in a fusion splicer [21] and adjusting arc current duration and power to melt the cladding structure while remaining distanced enough to prevent fusion with the solid-core fiber. In Fig.4.4

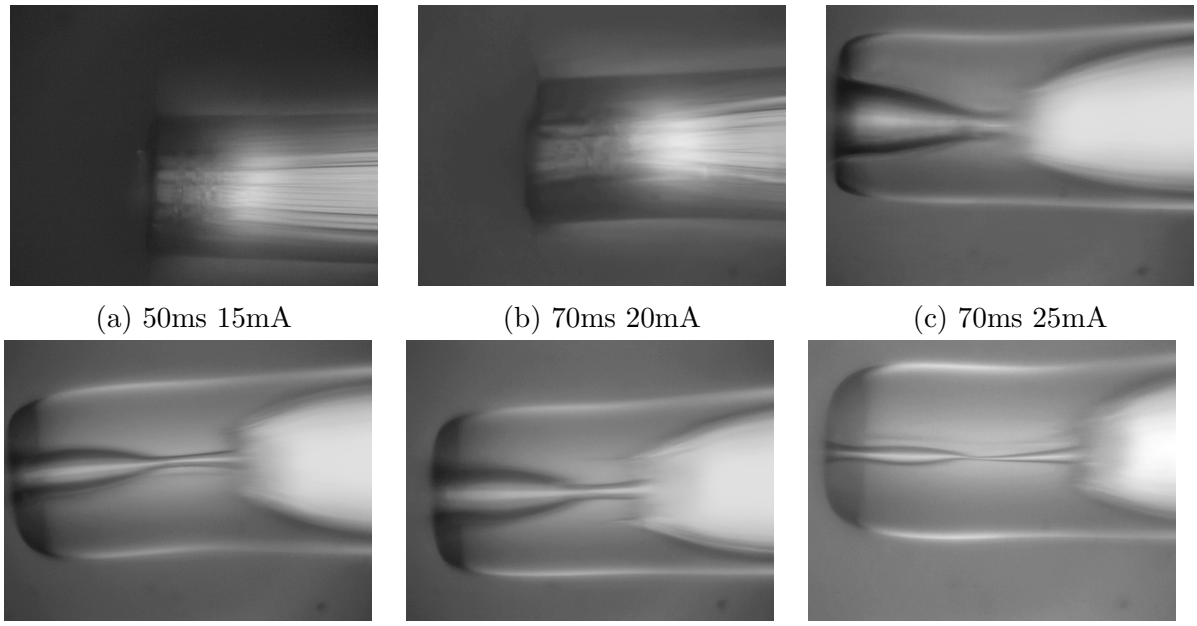

(a) 50ms 15mA (b) 70ms 20mA (c) 70ms 25mA

(d) 80ms 25mA (e) 90ms 25mA (f) 100ms 25mA

Figure 4.4: Side profile of collapsed cladding 1550HC fiber running the fiber splicer with varying current strength and duration. The solid-core fiber face was set at a distance of 18μm from the HCPBF face in the mechanical splicer.

the extent of collapse of the cladding is compared to various timing and power for an ORIENTEK T40 fusion splicer. The optimal setting is around an arc power of 25mA for a 70ms duration, though due to the imprecision in the arc power discharge the cladding on occasion will be overexposed, as shown in Fig.4.5.

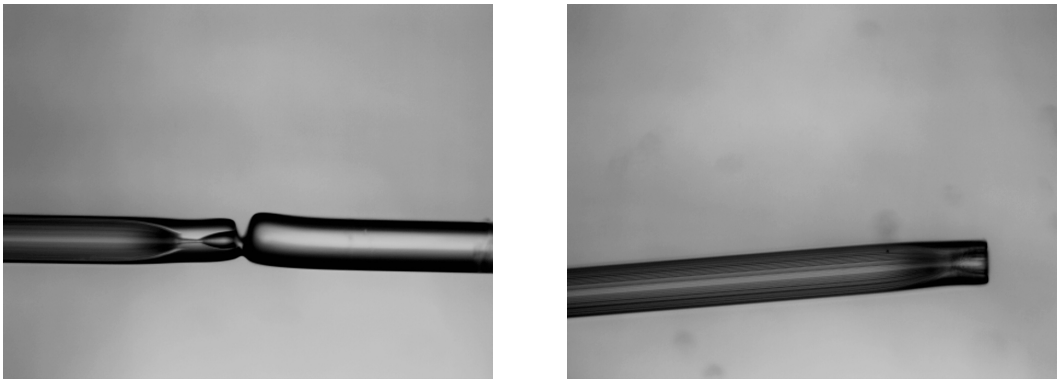

Figure 4.5: Variation between fibers using splicer settings 70ms 25mA.

Transmission

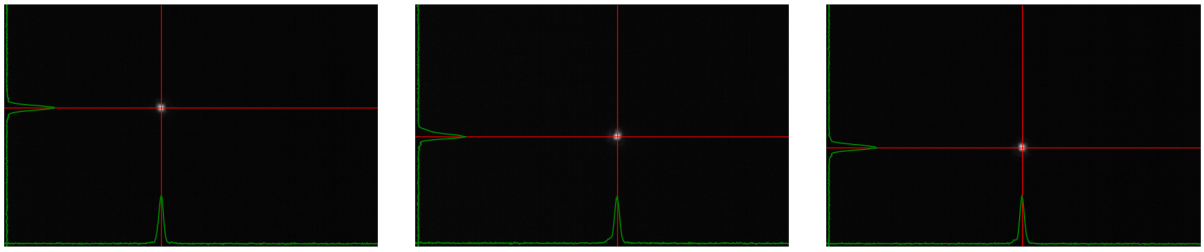

(a) (b) (c)

Figure 4.6: Modeshape of HC800B hollow-core fiber filled with (a)air (b)heavy water (c)DI water.

The air-filled 800nm HCPBF covers a transmission spectral range of 750nm–950nm. Light exits the fiber with a Gaussian mode shape, as shown in Fig.4.6. In a H_2O core, the coupling efficiency of the fiber drops to 31%, while a heavy water filled core is less affected by absorption over this region and retains a coupling efficiency of up to 67%.

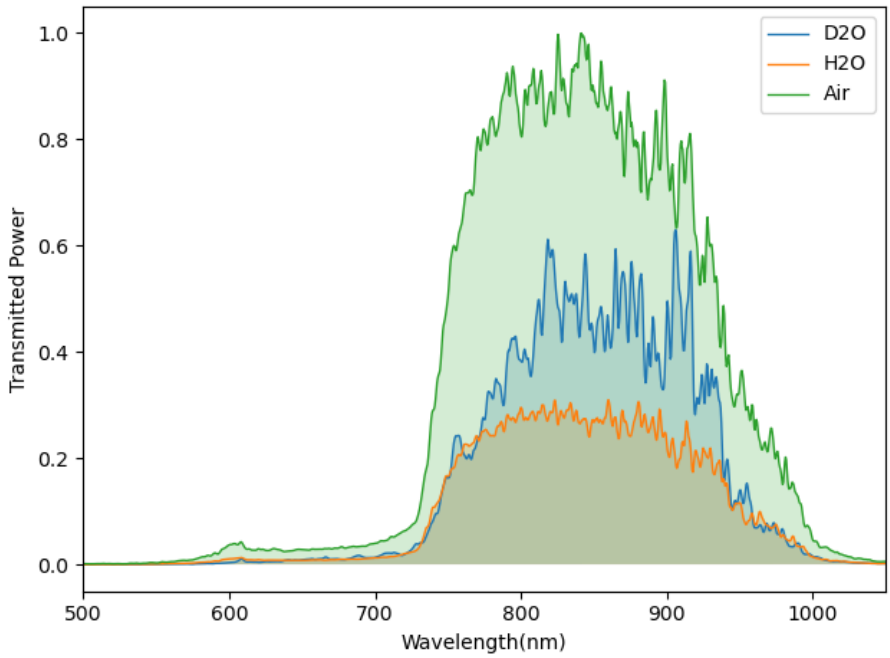

Figure 4.7: Transmission spectra of a 7 ± 0.6 cm long piece of HC800B selectively filled with H_2O(orange) and D_2O(blue). The vertical axis is normalized to the transmission of the empty HC800B fiber(green).

4.3 Full-Fiber Filling

Filling Method

The air in 1550nm HCPBF was replaced with deionized water and heavy water by utilizing capillary action.

Transmission

The air-filled 1550nm HCPBF covers a transmission spectral range of 1200nm–1700nm. With a filled core and cladding, the spectral range shifts to transmitting wavelengths between 600nm–1100nm for both heavy water and water, confirming the scaling laws. Heavy water achieved a coupling efficiency of 47%, but water only 16%. While the D_2O fiber modeshape retains a Gaussian profile, the H_2O mode shape contains noise as some

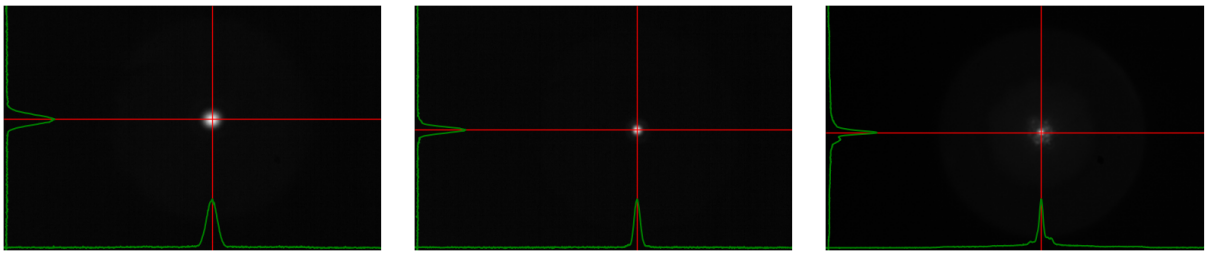

(a) (b) (c)

Figure 4.8: Modeshape of HC1550 fiber filled with (a)air (b)heavy water (c)DI water. Fiber filled with heavy water maintains a Gaussian profile while the fiber with regular distilled water shows some distortion.

light also leaks from the photonic structure. The absorption effects of H_2O severely reduce the transmission for wavelengths above 820nm, while compares well to the transmission of the D_2O fiber below 820nm and could arguably be used as a filling liquid.

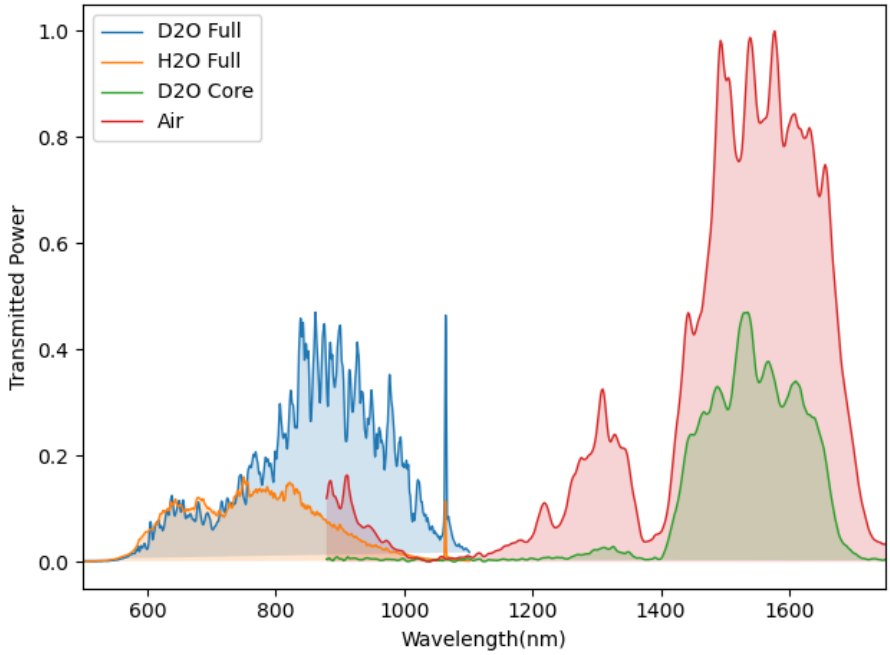

Figure 4.9: Transmission of H_2O and D_2O in fully-filled and core-filled HC1550 fiber 5cm in length.

Chapter 5

Indocyanine Green - Nanoparticles Suspended in HCPBF

Indocyanine green (ICG) - a fluorescent dye often used in microscopy imaging[34, 35] - was first used to test the guidance of fluorescence from nanoparticles suspended in solution within HCPBF. CNTs samples are seldom single-chirality, and there is a high chance that multiple chiralities will be present the solution. Isolating CNTs in solution will increase the dominance of the selected chirality but also requires an additional process. Before working with CNT samples, various fluorescent dyes were considered to use as a pseudo-CNT to mimic a single-chirality sample. ICG was chosen due to its excitation and emission wavelength overlap with the bandgap of fully-filled HC1550 and core-filled HC800B fibers.

ICG dye is an organic semiconductor with Homo-Lumo gap calculations estimating a 2eV energy gap, with variations depending on the solvent[27]. The HOMO and LUMO energy levels in organic semiconductors are parallel to the maximum valence and minimum conduction, and the aforementioned energy gap falls within the range of energy bandgaps found in inorganic semiconductors. The following section details the the optical properties of ICG and measurements of the optical properties when confined in HCPBF.

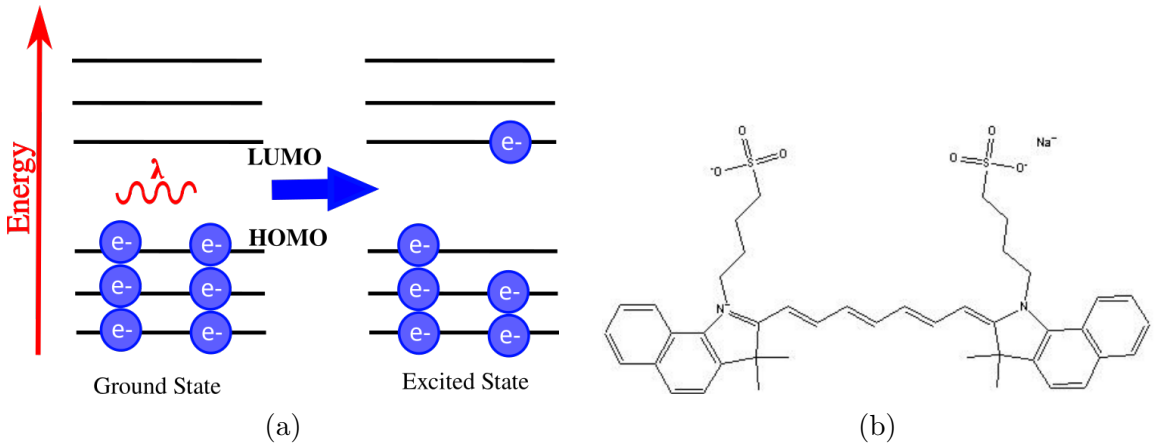

(a) (b)

Figure 5.1: (a) Depiction of the Homo-Lumo gap in organic semiconductors and the transition occurring between ground and excited states. (b) The chemical structure of ICG provided by MP Biomedicals.

5.1 Experiment Set-Up

The experimental set-up for the dye-filled HCPBF is very similar to that of the previously introduced HCPBF set-up, but includes a few additions. A fiber beam splitter was added between the fiber patch coming from the laser couplet and the bare fiber to monitor input power and wavelength. For fluorescence detection out of the fiber, a front-face fluorescence collection scheme was used and a long pass filter was placed in the path in order to filter out the incident light from the fluorescence. Additionally, a fiber clamp was placed on a translation stage to control the position and angle at which the bare fiber is positioned in the mechanical splicer chip. The prior development of these chips done by lab members of NPQO[20] tuned the fabrication recipe for coupling between 130μm to 125μm diameter fibers, specifically measuring the coupling between 800nm HCPBF to PM780HP fibers, resulting in a production of chips highly consistent in diameter. The 1550nm HCPBF however, has a diameter of 120μm. Mechanical splicer chips of 120μm to125μm diameter fibers are fabricated along with the 130μm to 125μm, but they are not of consistent quality and the majority of chips are over-exposed leading to the fibers to be loose and not level with each other in the chip. This resulted in average coupling rates of $> 10\%$ if supported by the chip structure only.

5.1.1 Sample Preparation

ICG powder was purchased from MP Biomedicals in quantities of 5mg per vial. A stock solution was made by dissolving 5mg of powder in 5mL of H_2O, then a low-concentration solution is made by diluting 10μL of stock solution into 2.5mL of either D_2O/H_2O. In a second approximate method for making low-concentration solutions, the tip of a syringe needle was use to scoop up a small amount of dye and then dissolve it in 5-10mL of D_2O/H_2O, working by eye based on the hue and opacity of the dye sample (See Fig.5.2(c)). The absorption of the sample was then measured in a cuvette and fitted to the concentration-based absorption cross-section data to find the concentration of the sample.

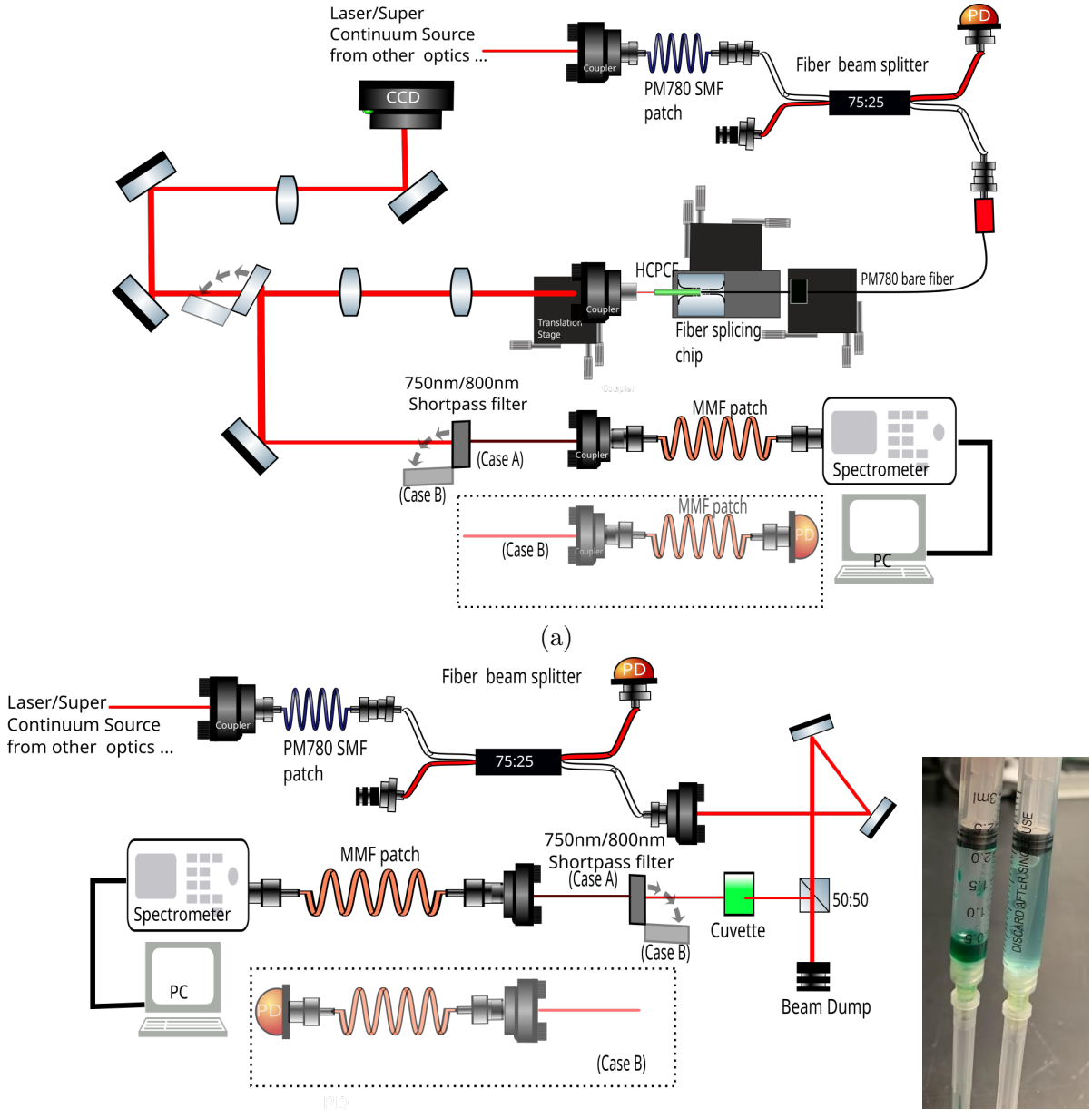

Figure 5.2: (a)Optical set-up to measuring output of the dye-filled fiber. The path to the CCD camera is used to monitor the modeshape coming out of the fiber. The path to the spectrometer (Case A) is used to measure the fluorescence spectrum and efficiency. The path to the photodiode (Case B) is used to measure the optical density of the fiber. (b)Optical set-up to measuring output of the dye in a 1cm cuvette. (c)Color and opacity difference between the stock solution (left) and diluted solution(right).

5.2 Absorption Cross-Section

ICG absorbs wavelengths between 600-900nm. The absorption is largely bimodal, with the greatest excitation occurring at 780nm and 700nm, but transforms into a monomeric distribution at 780nm at low concentrations and 700nm at high concentrations.

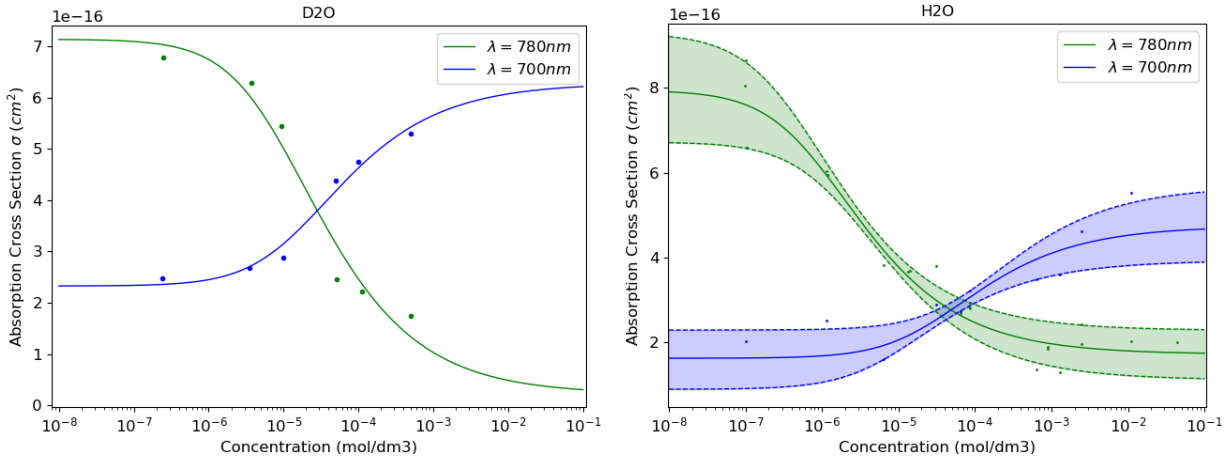

(a) (b)

Figure 5.3: Absorption cross-section at peak wavelengths 700nm(blue) and 780nm(green) for ICG dissolved in D_2O(a) and H_2O(b) . Data from [28] was fitted using a linear regression model.

Due to the chemical formation of ICG, the absorption of the molecule when dissolved in a solvent is highly concentration-dependent. ICG is made up of monomers, which are a type of molecule that can react with other monomers to form polymer chains. In the case of ICG, its monomers react with each other to form dimers, a chain of two joint monomers. With higher concentrations monomers are closer to each other, causing the molecules to have an increased likelihood to shift from monomers to dimers, which in turn are less likely to be excited and shift the center absorption wavelength. The concentration of monomers M to dimers D is governed by the equilibrium reaction:

$$M + M \rightleftarrows D \tag{5.1}$$

and law of mass action relation concentration

$$[D] = K_D[M]^2 \tag{5.2}$$

where K_D is the dimerization constant. Written in terms of concentration C and mole fractions, $[M] = x_M C = (1 - x_D)C$ and $[D] = \frac{x_D}{2}C$, the mole fraction of dimers can be written in terms of the dimerization constant and concentration.

$$x_D = 1 + \frac{1}{4K_D C} - \sqrt{\left(1 + \frac{1}{4K_D C}\right)^2 - 1} \tag{5.3}$$

The absorption cross-section model for ICG[30, 32] will be an average of the effects of the of monomers and dimers, where σ_M and σ_D are the monomer and dimer absorption cross-sections respectively.

$$\sigma = x_M \sigma_M + x_D \sigma_D = \sigma_M - x_D(\sigma_M - \sigma_D) \tag{5.4}$$

Plugging (5.3) into (5.4), remaining parameters can be found by doing a linear regression fit to absorption cross-section vs. concentration data from literature. The expected absorption cross-section can be calculated for any concentration. For ICG dissolved in H_2O, the existing literature presents some variation and so the upper/lower bounds and average were taken, while data for ICG dissolved in D_2O was based on [28]. The behavior in H_2O and D_2O are quite similar and are plotted in Fig.5.3. At lower concentrations the absorption cross-section is slightly greater for D_2O than H_2O, with the reverse for high concentrations.

$\lambda_{peak} = 780nm$	K_D	σ_M	σ_D
[28]	$6.01x10^5$	$9.29x10^{-16}$	$2.28x10^{-16}$
[29]	$1.03x10^5$	$6.74x10^{-16}$	$1.54x10^{-16}$
[30]	$1.40x10^5$	$6.72x10^{-16}$	$1.11x10^{-16}$
Average	$3.06x10^6$	$7.94x10^{-16}$	$1.72x10^{-16}$

Table 5.1: Absorption Cross Section parameter fitting of ICG dissolved in DI water. Fitting done with linear regression on σ vs. concentration data measured at $\lambda = 780nm$ from literature.

$\lambda_{peak} = 700nm$	K_D	σ_M	σ_D
[28]	$3.00x10^3$	$2.29x10^{-16}$	$25.68x10^{-16}$
[30]	$3.06x10^4$	$8.89x10^{-16}$	$3.93x10^{-16}$
Average	$9.31x10^3$	$1.62x10^{-16}$	$4.74x10^{-16}$

Table 5.2: Absorption Cross Section parameter fitting of ICG dissolved in DI water. Fitting done with linear regression on σ vs. concentration data at $\lambda = 700nm$ from literature.

λ_{peak}	K_D	σ_M	σ_D
$780nm$	$3.22x10^4$	$7.14x10^{-16}$	$2.68x10^{-17}$
$700nm$	$1.67x10^4$	$2.833x10^{-16}$	$6.28x10^{-16}$

Table 5.3: Absorption Cross Section parameter fitting of ICG dissolved in heavy water. Fitting done with linear regression on σ vs. concentration data at $\lambda = 700nm$ and $\lambda = 780nm$ from [28].

5.2.1 Photostability

At high concentrations, ICG behaves as a "J-aggregate", a category of dyes that shift in the absorption band to larger wavelengths in certain solvents. When mixed into water and other solvents, ICG shifts over time to a center wavelength of 893nm. This process can be accelerated under high heat. In high-concentration forms (in the range of 1000ppm solutions) [31], J-aggregates can be stored at room temperature for several months. However, in such a state the dye will be too optically dense to observe any optical excitation and when diluted to perform such measurements, the J-aggregates will begin to detach into smaller molecules within 24hrs. The effects of dye concentration on storage life in aqueous solutions becomes a tricky balance at single-digit ppm concentrations. At that concentration, the fluorescence intensity of the dye is at its greatest but it degrades to undetectable levels in just a couple of hours under optimal storage conditions[29, 33]. The rate of deterioration occurs linearly based on the initial concentration of ICG[28], but the amount of light exposure of the solution will also exasperate the degradation rate[33].

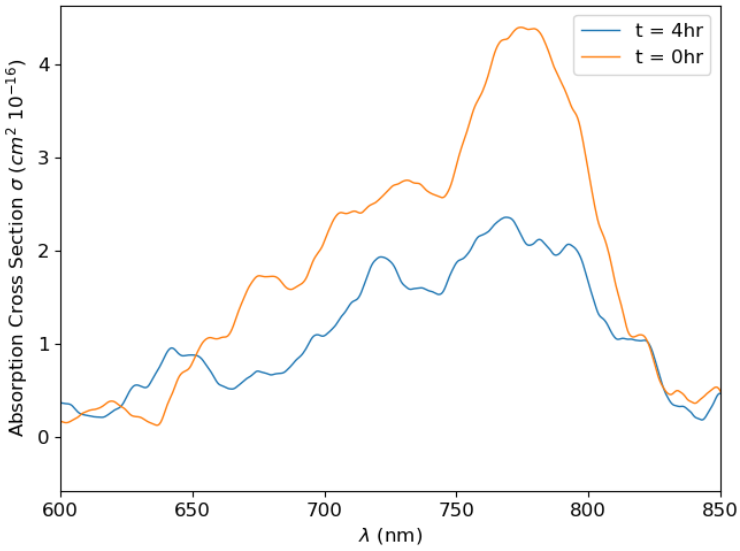

Figure 5.4: Degradation of a 4.5ppm initial concentration sample after 4hrs of light exposure reduced to a 2ppm concentration.

5.3 Fluorescence

5.3.1 ICG at Low Concentrations

Photoluminescence in the dye is observed in the range of 750-900nm, therefore overlapping with the absorption spectrum. The peak emission wavelength for ICG varies within 800nm-820nm[32, 33] when excited at 780nm, and decreases as solution concentration increases. The dimerization effects are attributed to (a) the formation of weakly fluorescent ICG molecular aggregates at high concentrations (b) self-quenching and (c) re-absorption of the emitted fluorescence by the ICG molecules due to overlap of the absorption and emission spectra. In the J-aggregate form the excitation wavelength shifts to 834nm and the emission peaks at 890nm although low quantum yield and strong light scattering does not lend to accurate measurements[31].

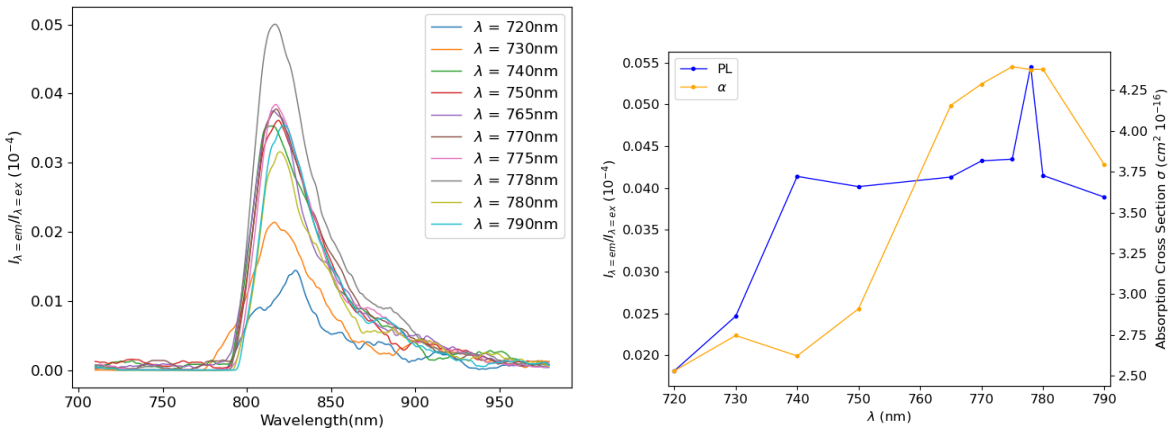

(a) (b)

Figure 5.5: A 4.5ppm sample of ICG dye was placed in a 1cm cuvette and characterized. (a)Fluorescence spectrum of 4.5ppm sample (b) Maximum fluorescence and maximum absorption spectrum of 4.5ppm sample with a pump power of 1mW at each wavelength.

5.3.2 ICG in HCPBF

Low-concentration samples of dye were prepared and used it to fill a 800nm HCPCF core and 1550nm HCPBF core and cladding. The measured absorption cross-section of the dye, shown in Fig.5.6, presents additional absorption effects caused by the fiber, notably the narrower bandgap of the 800nm HCPBF. Additionally, there is an observed 18nm shift in the peak absorption from 778nm to 796nm in the 1550nm bandgap-shifted liquid-filled fiber, while the 800mn liquid-core fiber has an insignificant 4nm shift in peak from 775nm to 771nm.

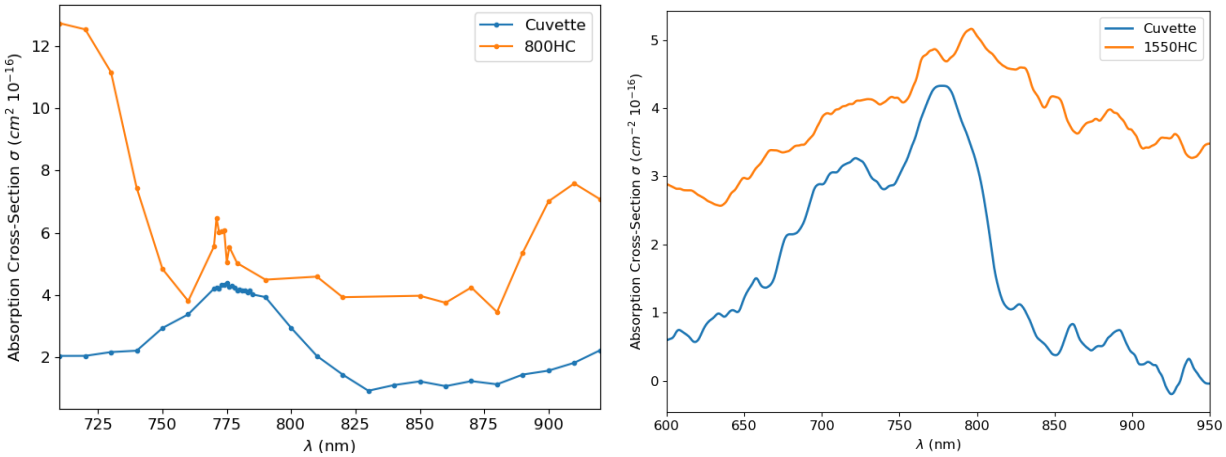

(a) (b)

Figure 5.6: Absorption cross-section of ICG samples (a) 2.5 ppm concentration in core of 800nm HCPBF and (b) 4 ppm concentration in core an d cladding of 1550nm HCPBF.

For 800nm core-filled HCPBF, ICG solutions were prepared with H_2O and D_2O solvents, but fluorescence was only guided in the D_2O. In the 800HC fiber there was already significant loss coming from the narrow bandgap in combination with lower refractive index contrast of using a liquid medium, as half of the absorption spectrum is outside the bandgap; The absorption of effects of H_2O in the NIR (discussed in chapter 2) and re-absorption from the overlapping excitation-emission spectra is suspected to be greater than the number of emitted photons. The fluorescence guided in the 800nm HCPBF was also influenced by the bandgap, shown in Fig.5.8b. The emission had a large shifts in peak for excitation between $745-775$nm - wavelengths at the edge of the bandgap and with high

absorption effects - varying peak fluorescence between 800 and 820nm while for excitation above 775nm the fluorescence stayed centered at 805nm.
Fluorescence was also in ICG-filled 1550nm HCPBF with D_2O as solvent, which had the best ratio of fluorescence intensity to emission intensity ("fraction of fluorescence"). For a 4ppm ICG sample the fraction of fluorescence are compared in Fig.5.7 for excitation wavelengths below the emission wavelength range. The peak fluorescence in the cuvette was at 820nm, but was shifted down 10nm to 810nm in the fiber and the fraction of fluorescence in 1550nm HCPBF was $\sim$ 35x greater than that measured through the cuvette. For the 3.7ppm sample in core-filled 800nm HCPBF similar fraction of fluorescence to the cuvette sample were measured at the excitation wavelength of peak absorption(778nm).

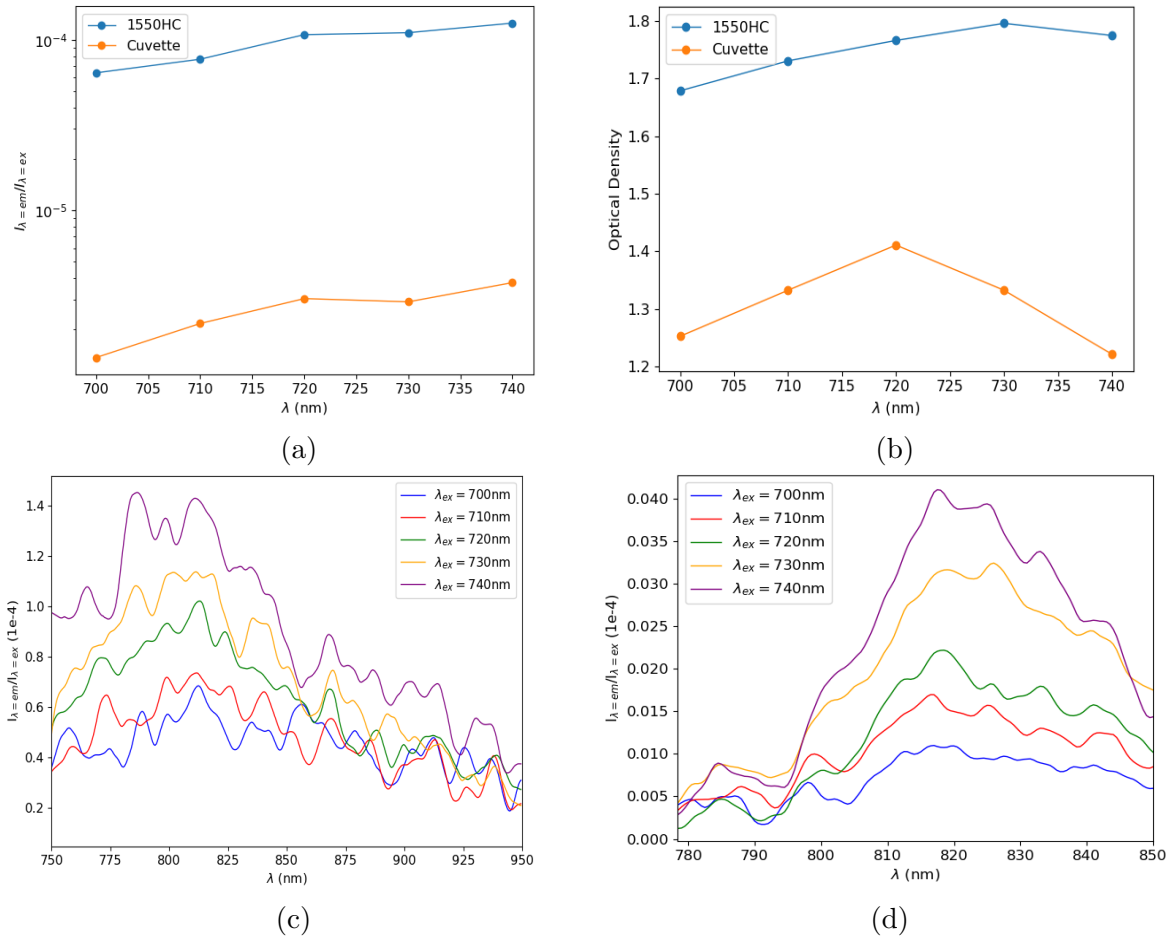

Figure 5.7: (a) The maximum fraction of fluorescence is plotted against excitation wavelength for a 4ppm ICG sample in a 1cm piece of 1550nm HCPBF and 1cm cuvette. The maximum fraction of fluorescence of the ICG in the cuvette is only 4% of that measured in fiber. (b) The optical density at each excitation wavelength. The fraction of fluorescence spectrum of the 4ppm ICG solution in (c) 1550nm HCPBF (d) a cuvette.

At the maximum absorption wavelength, the fraction of fluorescence and output power at the excitation wavelength are measured as a function of the input power, shown in Fig.5.8c. The fraction of fluorescence peaks at an input power of $50\mu W$, while the output power increases logarithmically and appears to approaching a limit on the transmission. Overall, the fluorescence efficiency is of 0.00051% in the 800nm HCPBF $\lambda_{ex} = 778$ and for 1550nm HCPBF 0.014% at $\lambda_{ex} = 740$nm, which is comparable to other optofluidic waveguides [42].

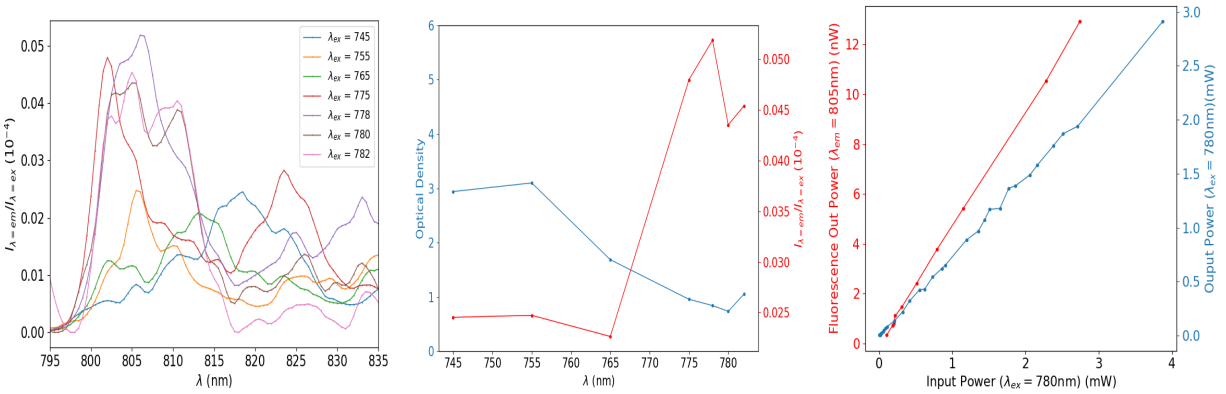

(a) (b) (c)

Figure 5.8: Measurements of 3.7ppm ICG sample in a 2cm piece of core-filled 800nm HCPBF (a) The fraction of fluorescence spectrum (b) The maximum fraction of fluorescence and optical density against excitation wavelength. (c) Measured output peak power and fractional fluorescence as a function of input power.

Chapter 6

Liquid-Suspended CNT Experiments

6.1 HCPBF Bandgap Overlap with CNT Excitation and Emission

To successfully collect the CNT fluorescence when suspended within a HCPBF, the particle emission and excitation must be within the bandgap of the fiber. Taking the most commonly available HCPBFs, Table 4.1 shows the bandgap range and the central operating wavelengths for core-filled and fully D_2O-filled fibers. In Fig.6.1, the liquid-filled HCPBF bandgaps are overplayed with the excitation and emission spectrums of CNTs calculated in the previous section. From this overlay, it appears that 10 chiralities of CNTs fall within the bandgap of a fully-filled 1550nm HCPBF and one within the bandgap of fully-filled 1060nm HCPBF. The potential CNT candidates and their characteristics are listed in Table 6.2 along and their spectrum plotted within the 1550nm fully-filled bandgap in Fig.6.2.

HCPBF	Central Wavelength Air (nm)	Central Wavelength D_2O (nm)	Bandwidth (nm)
HC2000	2000	1144	250
HC1550	1550	887	500
HC1060	1060	606	100
HC800B	800	457	200

Table 6.1: Thorlabs fiber bandgap shift. The ranges for HC1550 and HC800B are approximated from spectrum measurements and HC2000 and HC1060 are taken from NKT datasheets[70, 71].

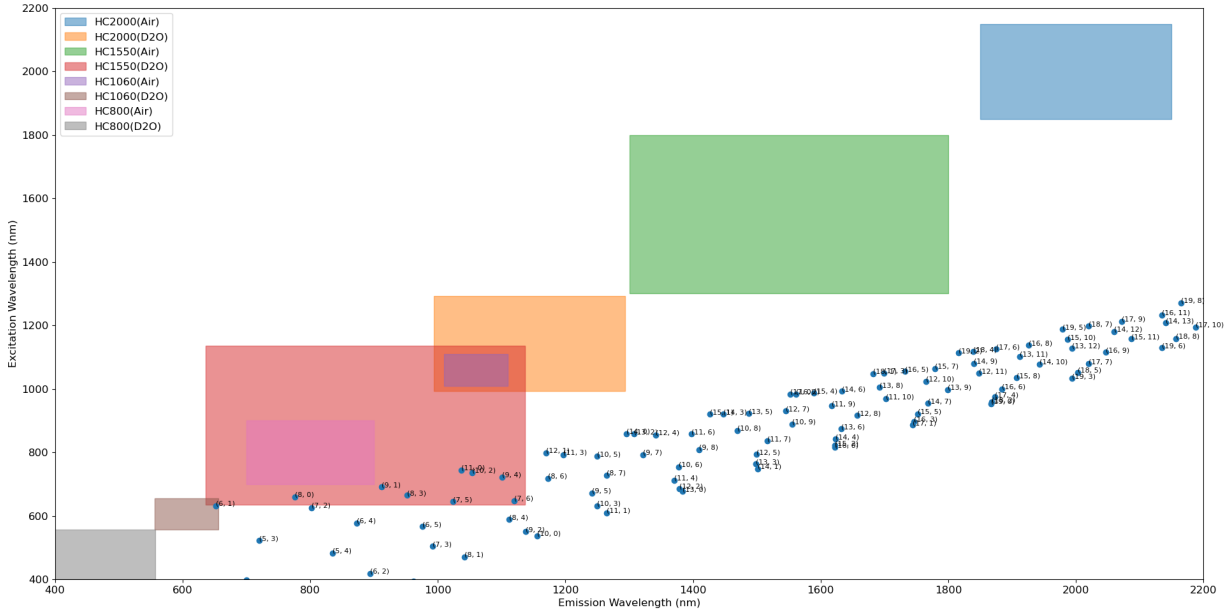

Figure 6.1: Hollow-core fiber bandgap overlayed on CNT emission vs. excitation wavelengths

QuIN Lab at the University of Waterloo has developed a CNT isolation process using the surfactant sodium deoxycholate (DOC) in DI water, and are able to produce samples with (7, 6) and (7, 5) dominant samples. Thus far an experiential set-up for characterizing the CNT samples was completed, but use of the sample in HCPBF has not yet been completed. The sample information that has so far been collected is included.

(n, m)	dt (nm)	Θ (deg)	λ_{11} (nm)	λ_{22} (nm)
(6, 1)	0.52	0.13	652.62	631.79
(7, 2)	0.65	0.21	802.05	625.92
(7, 5)	0.83	0.43	1023.74	645.33
(7, 6)	0.89	27.46	1119.76	647.64
(8, 0)	0.64	0	776.01	660.25
(8, 3)	0.78	0.27	951.61	665.39
(9, 1)	0.76	0.09	912.1	691.29
(9, 4)	0.92	0.31	1100.63	722.39
(10, 2)	0.88	0.16	1053.43	736.68
(11, 0)	0.87	0	1036.93	744.57

Table 6.2: CNTs with emission and excitation transmittable through HC1550 filled with D_2O.

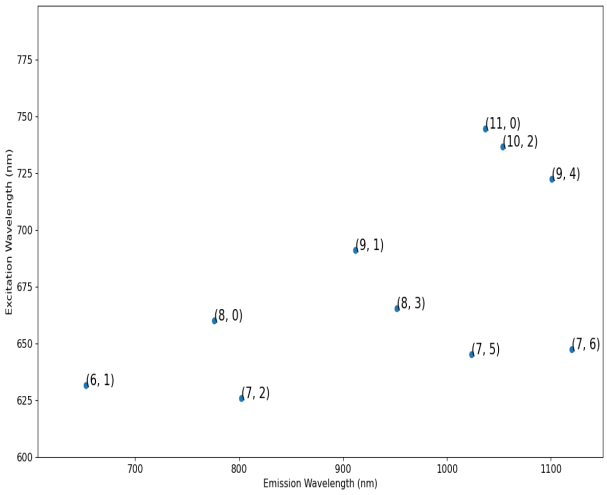

Figure 6.2: Excitation/Emssion spectrum of CNTs falling within the D_2O-filled 1550HCPBF bandgap.

6.2 Experiment Set-Up

Due to the absence of a tunable, few nanometer linewidth light source available in the NPQO lab for excitation wavelengths between $600 - 700$nm, one was made by passing a super continuum source through a 1800g/mm diffraction grating and filtering through an optical slit. From this set-up, depicted in Fig.6.3, a pump power of 48μW was achieved for a linewidth of $= 1.838 \pm 0.004$nm, tunable over the required excitation bandwidth. For cuvette measurements, the set-up was modified as shown in Fig.6.4 and used to measure absorption and fluorescence of the sample .

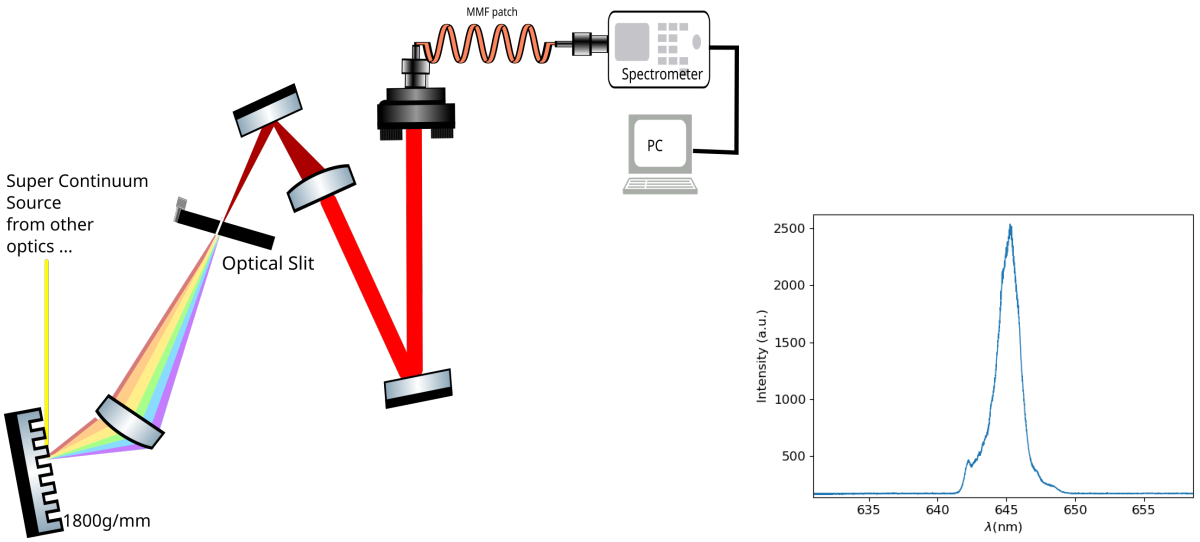

(a) (b)

Figure 6.3: (a) The experiential used set-up for filtering and selecting the pump source wavelength from the super continuum source. (b)The spectrum and intensity of the excitation beam at $\lambda = 645$nm picked-offed the super continuum source. The power measures 48μW and fwhm$= 1.838 \pm 0.004$nm.

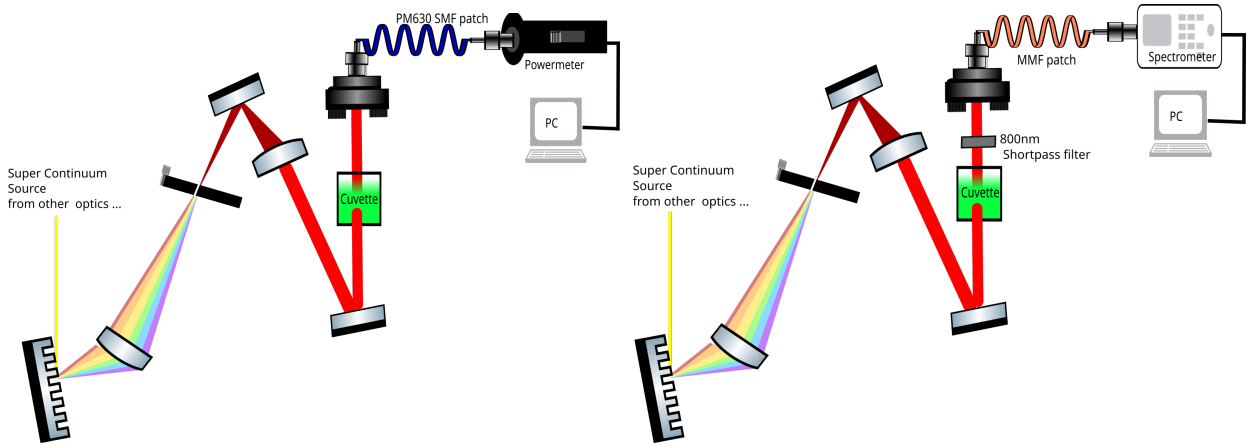

Figure 6.4: The experiential used set-up for measuring (a)Absorption and (b) Fluorescence of CNT samples in a cuvette.

6.3 Sorted CNT sample

Sample History

CNT samples were prepared by HeeBong Yang from the QuIN Lab at the University of Waterloo. SG65i powder was purchased from Sigma Aldrich and dispersed in a surfactant at an initial powder concentration of 1 mg/mL. The sample then underwent a procedure of purification steps, sorting with polymers & surfactants, and polymer exchange. The final condition of the sample was 65% (7,5), (7,6) dominant SWCNTs in DI water with 0.04% DOC, but at an unknown concentration.

Figure 6.5: Sorted (7,5), (7,6) dominant CNT sample. Solution appears to have a green hue.

6.3.1 Sample Characteristics

CNT solutions follow Beer-Lambert's Law [74, 77], $A = log(\frac{I_{in}}{I_{out}}) = \varepsilon CL$ so the concentration can be deduced from the measured absorbance. Fig.6.6(a) and the average previously reported extinction coefficient[75, 76, 77] $\varepsilon = 30.98$ mL mg^{-1}cm^{-1} estimate a sample concentration around 0.0042 ± 0.0007 mg/mL. Unfortunately no PL was detected from the sample. The sample was then diluted in 4 steps of serial dilution in order to confirm that the lack of fluorescence was not due to interference between CNTs due to the concentration of the sample. However, as shown in Fig.6.7(a), the absorbance of the diluted samples diminishes indicating that the initial concentration sample was not at a quenching concentration. From Fig.6.7(b), the initial concentration CNT sample transmitted power appears linear, indicating that the sample absorbance had not yet reached the saturation point. From Fig.6.9(b), the first-step and second-step diluted samples transmitted power appear linear, indicating that the sample absorbance had not yet reached the saturation point.

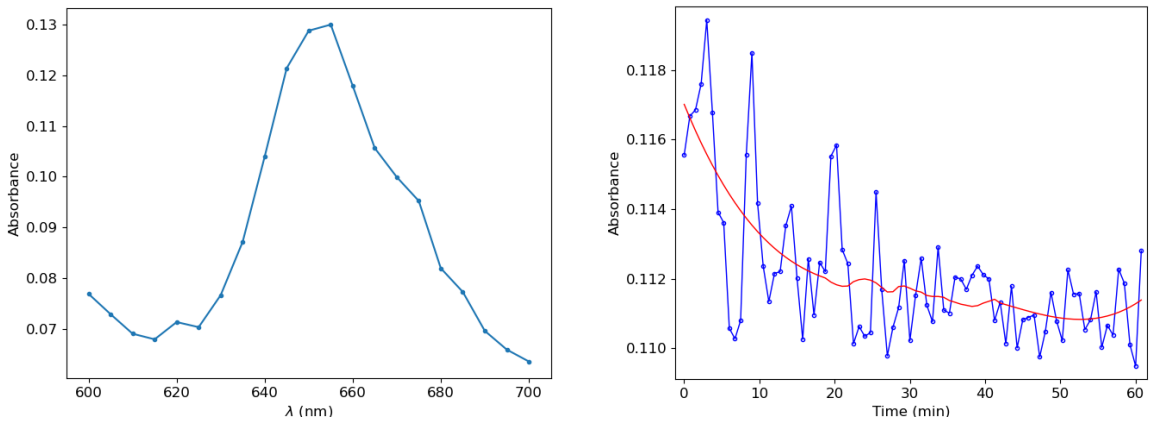

(a) (b)

Figure 6.6: (a) Absorbance spectrum of CNT sorted CNT sample (b)Absorbance of CNT sorted sample over 60 minutes, the absorbance of the sample stabilizes after 30 minutes.

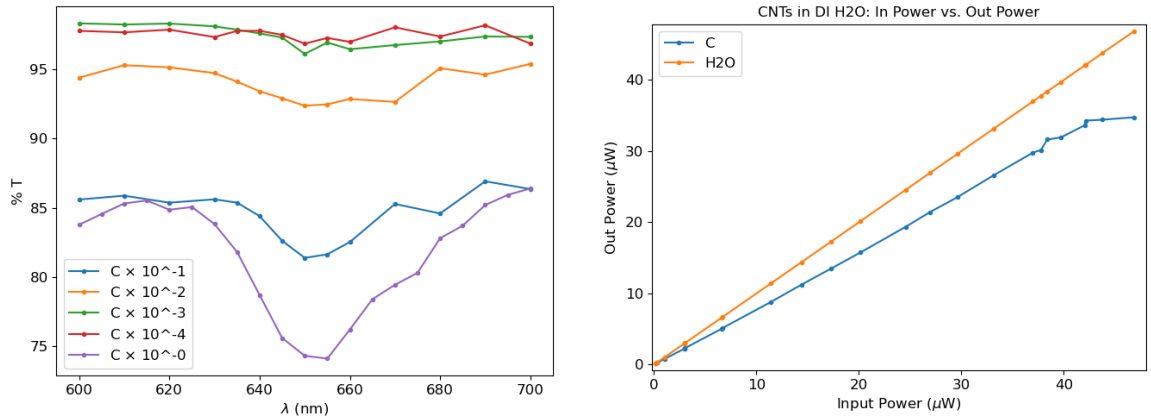

(a) (b)

Figure 6.7: (a) Serial Dilution of the original concentration "C" sample. All diluted samples have a lower difference in absorbance between the expected peak absorbance wavelength and surrounding wavelengths. (b) The power saturation of the CNT solution compared to deionized water. The output power remains linear to the input power indicating the saturation threshold has not yet been reached.

6.4 Unsorted CNT sample

Despite the high absorption loss from DI water in the excitation wavelength range, fluorescence has been detected for these chiralities of CNTs suspended in DI water before[73], though there is 23.25% pm 10% decrease in PL intensity when using H_2O instead of D_2O for (7, 5) and 42.5% pm 5% for (7,6) and quantum yields are expected to be around 1.04% and 1.40% respectively. To remove the absorption effects of DI water, measurements were repeated on a D_2O-based sample. Unfortunately, a sorted D_2O-based sample was unable to be prepared due to the need to develop a new sorting recipe coupled with minimum requirement of 50mL - 100mL of solution to carry out the CNT sorting procedure. Since the amount of D_2O available at the time of the experiment was limited, only an unsorted sample of CNTs in D_2O was prepared.

Sample History

CNT samples at the initial concentration were prepared by HeeBong Yang from the QuIN Lab at the University of Waterloo. SG65i powder was purchased from Sigma Aldrich and dispersed in D_2O at a concentration of 1mg/mL. The sample was then serially diluted from the initial concentration four times.

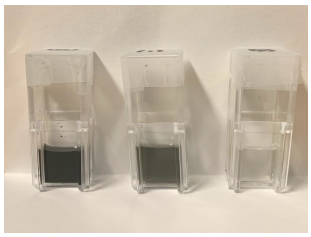

Figure 6.8: Unsorted CNT sample. (left) The initial concentration "C" CNT sample, black in color. (center) The first-step dilution sample, $0.1C$, gray in hue. (right) The second-step dilution sample, $0.01C$, a clear liquid.

Sample Characteristics

The absorbance of each sample concetration was measured, as shown in Fig. 6.9(a). The initial concentration sample had near-zero transmission, being too dense of a concentration to see any discernible optical features, while the third and fourth-step diluted samples were near-complete transmissible, having too low of a CNT concentration to measure any discernible optical features. The first and second-step diluted samples each a have

discernible absorbance spectrum that agree with the sorted sample absorbance spectrum, with the second-step dilution sample being closest in transmission to the sorted sample. Unfortunately, there was also no fluorescence detected from any of the D_2O CNT sample concentrations either, indicating that the high absorption effects of H_2O are at least not the main factor in inhibiting the detection of fluorescence from the CNTs. Further investigation still remains.

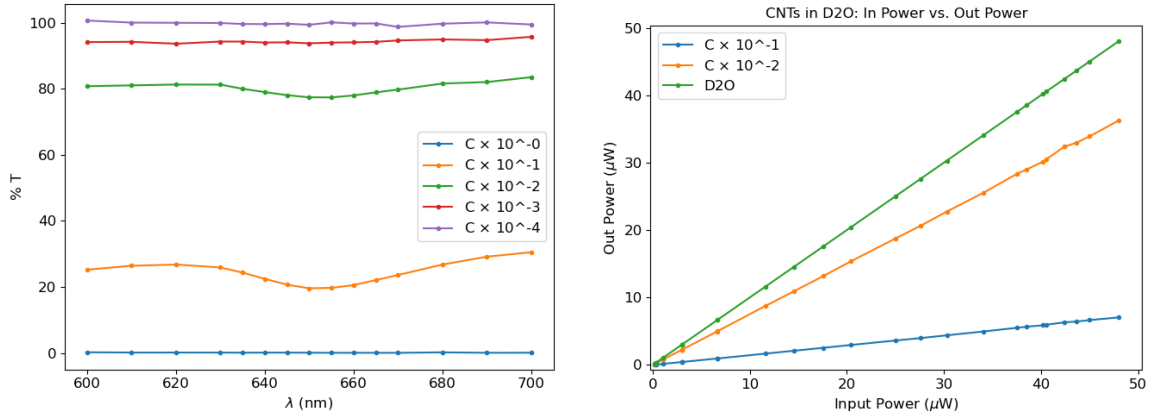

(a) (b)

Figure 6.9: (a) Transmission spectrum of the diluted samples from the original concentration,"C", sample. The first and second step dilutions have discernible absorbance peaks corresponding to (7, 5) and (7, 6) dominant CNTs. (b) The power saturation of the first and second step CNT dilutions compared to D_2O. The output power remains linear to the input power indicating the saturation threshold has not yet been reached.

6.5 CNTs in HCPBF

Despite the absence of detected fluorescence from the above sample measurements, the absorbance measurements confirm the presence and dominance of (7,6) and (7,5) type CNTs in the samples. The sorted CNTs dispersed in H_2O sample was used to fill a 2cm piece of HCPBF and the transmission spectrum measured, as shown in Fig. 6.11.
The CNT-HCPBF measurements show inconclusive results however due to a transmission efficiency of less than 0.015%. Using HC1550 HCPBF required 120μm-125μm splicing chips, but a successful fabrication recipe has not yet been tuned to these smaller-diameter chips, resulting in poor coupling into the HCPBF.

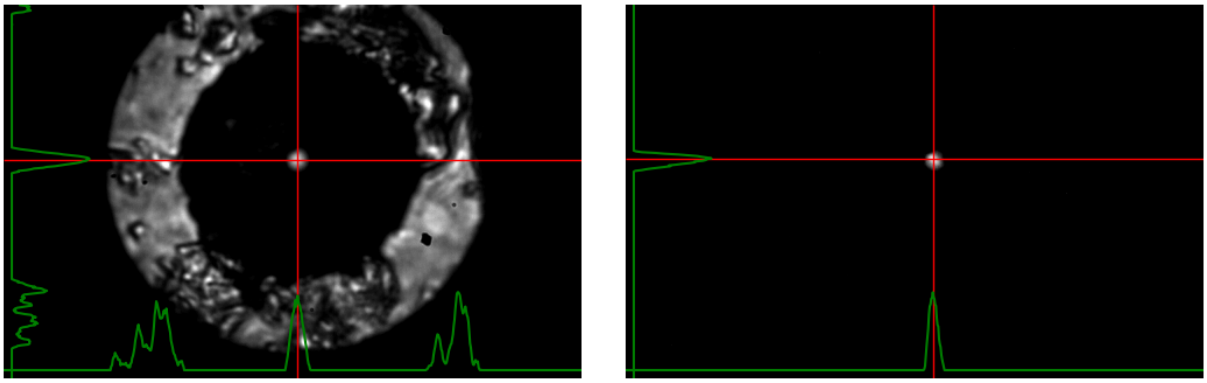

(a) (b)

Figure 6.10: Modeshape of the selected CNT sample-filled HC1550 HCPBF. (a)The modeshape of the fiber measured with the SCS. While modeshape corresponding to light guided through the core indicates a Gaussian modeshape, the majority of the light is coupled into the cladding of the fiber. (b) The modeshape of the fiber measured with a single wavelength source at 852nm.

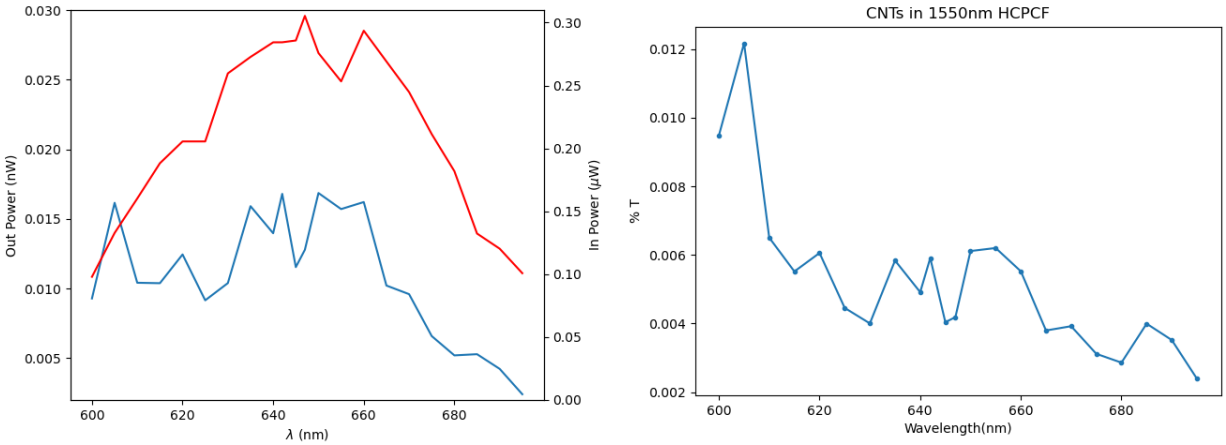

(a) (b)

Figure 6.11: Measurements of the sorted CNT sample-filled HC1550 HCPBF. (a) The spectrum for pump power (red) into the fiber-integrated sample and output power (blue) measured through the fiber integrated sample. (b) The transmission spectrum.

Chapter 7

Conclusion

In this thesis use of HCPBFs as a liquid-waveguide was studied. The preservation of light bandgap guidance through liquid demonstrated by experimentally confirming the scaling laws for liquid-filled fibers of H_2O and D_2O. The main results of the thesis were obtained in the measurements of the interaction of suspended ICG particles within the mode of the fiber. The dye molecules were excited in the fiber and fully-filled HCPBF guiding light via optical bandgap exhibited a higher efficiency than that seen in the liquid-core fiber. Despite difficulty with the coupling, there is high enough efficiency the potential of creating fluorescent light sources. However, using organic molecules becomes troublesome due to rapid degradation and photobleaching. Semiconducting CNTs in theory can also be used as a fluorescent medium, removing the lifespan issues of organic dyes and and increased tunability through chirality selection processes. The overlap in certain chirality CNT spectrums and the bandgap of commercially available HCPBF when filled with heavy water makes further study into their integration warranted.

Future Work

While the results of suspended ICG particles are promising and show a proof-of-concept, the progression to suspended CNTs in HCPCF is incomplete. The initial tests with a sorted CNTs sample were inconclusive and further investigation is needed to produce a fluorescent sample. Future experimental efforts will hopefully lead to uses of CNTs in fiber-integrated devices. Besides the CNT samples, one of the main challenges that remains is obtaining a consistent and high coupling to the HC1550 HCPCF. Butt-coupled mechanical splicing chips fabricated for HC800 HCPCF consistently achieve coupling around 75-80% and robustly hold the fibers together[20], but the same recipe does not produce high-fidelity butt-coupled mechanical splicing chips for 1550nm HCPCF. This is another avenue that

needs to be explored but it is likely to be solved with modest efforts.
After the implementation of the aforementioned improvements, future prospects include integrating the suspended particle-filled HCPCF into a narrow linewidth external cavity semiconductor laser (NLECSL) as a gain medium. A potential NLECSL set-up using the common Littrow configuration depicted in Fig.7.1(a). Narrow line-width dye lasers have

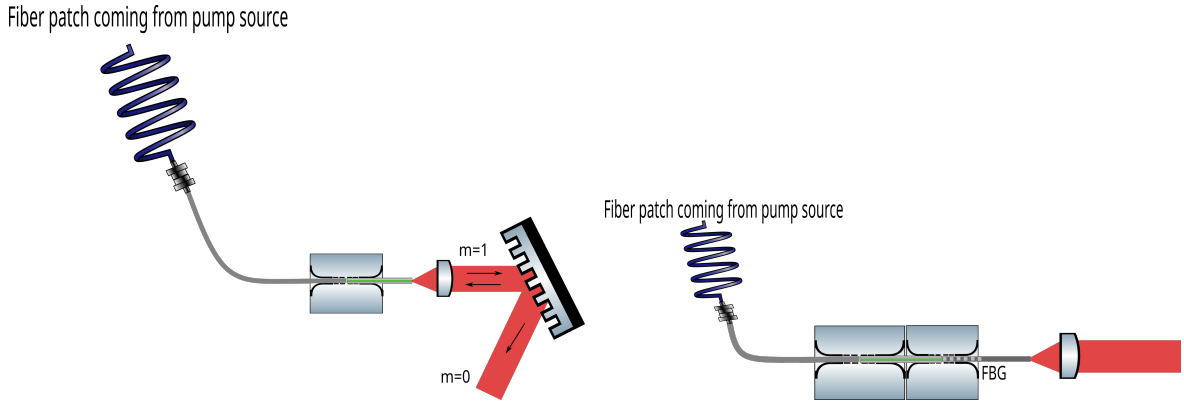

Figure 7.1: Example NLECSL configurations integrating the liquid-HCPCF as the gain medium (a) Littrow configuration (b) Single-wavelength fiber-integrated approach with FBG.

already been made using liquid dyes as gain medium[81, 80] with applications nonlinear[83] and atomic optics[84] . With organic dyes like ICG having wide fluorescence spectrum a tunable laser is desirable, but CNTs typically have fluorescence linewidth around 4-6nm when isolated and 20nm in bulk samples[78] will have promise in a fixed-wavelength cavity. For single-wavelength laser configurations, fiber-integrated systems have been demonstrated using fiber Bragg-gratings as end-reflector of an external cavity system[79]. An easy integration if using fiber splicing chips Fig.7.1(b).

References

[1] Pochi Yeh, Amnon Yariv, and Emanuel Marom. Theory of bragg fiber. J. Opt. Soc. Am., 68(9):1196–1201, Sep 1978.

[2] R. K. Chourasia and V. Singh, "Estimation of photonic band gap in the hollow core cylindrical multilayer structure," Superlattices and Microstructures, vol. 116, pp. 191–199, Apr. 2018, doi: 10.1016/j.spmi.2018.02.023.

[3] M. A. Duguay, Y. Kokubun, T. L. Koch, and Loren Pfeiffer. Antiresonant reflecting optical waveguides in SiO2- Si multilayer structures. Applied Physics Letters, 49(1):13–15, 1986.

[4] Delonge T, Fouckhardt H (1995) Integrated optical detection cell based on Bragg reflecting waveguides. J Chromat A 716:135–139

[5] D. Yin, H. Schmidt, J. P. Barber, and A. R. Hawkins, "Integrated ARROW waveguides with hollow cores," Opt. Express, vol. 12, no. 12, p. 2710, 2004, doi: 10.1364/OPEX.12.002710.

[6] F. Benabid, "Inhibited-coupling guiding hollow core photonic crystal fibers," in 2013 Conference on Lasers & Electro-Optics Europe & International Quantum Electronics Conference CLEO EUROPE/IQEC, Munich, Germany, May 2013, pp. 1–1. doi: 10.1109/CLEOE-IQEC.2013.6801305.

[7] S.-J. Im, A. Husakou, and J. Herrmann, "Guiding properties and dispersion control of kagome lattice hollow-core photonic crystal fibers," Opt. Express, vol. 17, no. 15, p. 13050, Jul. 2009, doi: 10.1364/OE.17.013050.

[8] F. Amrani et al., "Low-loss single-mode hybrid-lattice hollow-core photonic-crystal fibre," Light Sci Appl, vol. 10, no. 1, p. 7, Dec. 2021, doi: 10.1038/s41377-020-00457-7.

[9] H. Schmidt and A. R. Hawkins, "Optofluidic waveguides: I. Concepts and implementations," Microfluid Nanofluid, vol. 4, no. 1–2, pp. 3–16, Jan. 2008, doi: 10.1007/s10404-007-0199-7.

[10] D. Yin, D. W. Deamer, H. Schmidt, J. P. Barber, and A. R. Hawkins, "Integrated optical waveguides with liquid cores," Appl. Phys. Lett., vol. 85, no. 16, pp. 3477–3479, Oct. 2004, doi: 10.1063/1.1807966.

[11] H. Schmidt and A. R. Hawkins, "The photonic integration of non-solid media using optofluidics," Nature Photon, vol. 5, no. 10, pp. 598–604, Oct. 2011, doi: 10.1038/nphoton.2011.163.

[12] Yariv, Amnon and Pochi Albert Yeh, Optical Waves in Crystals: Propagation and Control of Laser Radiation,"1st ed. Wiley-Interscience, 2002.

[13] J. D. Joannopoulos, Photonic crystals: molding the flow of light, 2nd ed. Princeton: Princeton University Press, 2008.

[14] R. K. Chourasia and V. Singh, "Estimation of photonic band gap in the hollow core cylindrical multilayer structure," Superlattices and Microstructures, vol. 116, pp. 191–199, Apr. 2018, doi: 10.1016/j.spmi.2018.02.023.

[15] P. R. Villeneuve and M. Piche´, "Photonic band gaps in two-dimensional square and hexagonal lattices," Phys. Rev. B, vol. 46, no. 8, pp. 4969–4972, Aug. 1992, doi: 10.1103/PhysRevB.46.4969.

[16] R. F. Cregan et al., "Single-Mode Photonic Band Gap Guidance of Light in Air," Science, vol. 285, no. 5433, pp. 1537–1539, Sep. 1999, doi: 10.1126/science.285.5433.1537.

[17] I. A. Sukhoivanov and I. V. Guryev, Photonic Crystals: Physics and Practical Modeling, vol. 152. Berlin, Heidelberg: Springer Berlin Heidelberg, 2009. doi: 10.1007/978-3-642-02646-1.

[18] T. A. Birks, D. M. Bird, T. D. Hedley, J. M. Pottage, and P. St. J. Russell, "Scaling laws and vector effects in bandgap-guiding fibres," Opt. Express, vol. 12, no. 1, p. 69, 2004, doi: 10.1364/OPEX.12.000069.

[19] G. Antonopoulos, F. Benabid, T. A. Birks, D. M. Bird, J. C. Knight, and P. St. J. Russell, "Experimental demonstration of the frequency shift of bandgaps in photonic crystal fibers due to refractive index scaling," Opt. Express, vol. 14, no. 7, p. 3000, 2006, doi: 10.1364/OE.14.003000.

[20] R. A. Maruf and M. Bajcsy, "On-chip splicer for coupling light between photonic crystal and solid-core fibers," Appl. Opt., vol. 56, no. 16, p. 4680, Jun. 2017.

[21] L. Xiao, W. Jin, M. S. Demokan, H. L. Ho, Y. L. Hoo, and C. Zhao, "Fabrication of selective injection microstructured optical fibers with a conventional fusion splicer," Opt. Express, vol. 13, no. 22, p. 9014, 2005.

[22] S. Kedenburg, M. Vieweg, T. Gissibl, and H. Giessen, "Linear refractive index and absorption measurements of nonlinear optical liquids in the visible and near-infrared spectral region," Opt. Mater. Express, vol. 2, no. 11, p. 1588, Nov. 201

[23] M. Bajcsy et al., "Laser-cooled atoms inside a hollow-core photonic-crystal fiber," Phys. Rev. A, vol. 83, no. 6, p. 063830, Jun. 2011, doi: 10.1103/PhysRevA.83.063830.

[24] A. P. Hilton, C. Perrella, F. Benabid, B. M. Sparkes, A. N. Luiten, and P. S. Light, "High-efficiency cold-atom transport into a waveguide trap," Phys. Rev. Applied, vol. 10, no. 4, p. 044034, Oct. 2018, doi: 10.1103/PhysRevApplied.10.044034. A

[25] P. Domokos, P. Horak, and H. Ritsch, "Quantum description of light-pulse scattering on a single atom in waveguides," Phys. Rev. A, vol. 65, no. 3, p. 033832, Mar. 2002, doi: 10.1103/PhysRevA.65.033832.

[26] M. T. Manzoni, "New Systems for Quantum Nonlinear Optics,". 2017, Thesis, p. 39-40.

[27] X. Fang et al., "One-step condensation synthesis and characterizations of indocyanine green," Results in Chemistry, vol. 3, p. 100092, Jan. 2021, doi: 10.1016/j.rechem.2020.100092.

[28] W. Holzer et al., "Photostability and thermal stability of indocyanine green," Journal of Photochemistry and Photobiology B: Biology, vol. 47, no. 2-3, pp. 155-164, Dec. 1998.

[29] M. L. Landsman, G. Kwant, G. A. Mook, and W. G. Zijlstra, "Light-absorbing properties, stability, and spectral stabilization of indocyanine green," Journal of Applied Physiology, vol. 40, no. 4, pp. 575–583, Apr. 1976.

[30] M. Mauerer, A. Penzkofer, and J. Zweck, "Dimerization, J-aggregation and J-disaggregation dynamics of indocyanine green in heavy water," Journal of Photochemistry and Photobiology B: Biology, vol. 47, no. 1, pp. 68–73, Nov. 1998.

[31] F. Rotermund, R. Weigand, W. Holzer, M. Wittmann, and A. Penzkofer, "Fluorescence spectroscopic analysis of indocyanine green J aggregates in water," Journal of Photochemistry and Photobiology A: Chemistry, vol. 110, no. 1, pp. 75–78, Oct. 1997.

[32] R. Philip, A. Penzkofer, W. Bäumler, R. M. Szeimies, and C. Abels, "Absorption and fluorescence spectroscopic investigation of indocyanine green," Journal of Photochemistry and Photobiology A: Chemistry, vol. 96, no. 1–3, pp. 137–148, May 1996.

[33] V. Saxena, M. Sadoqi, and J. Shao, "Degradation Kinetics of Indocyanine Green in Aqueous Solution," Journal of Pharmaceutical Sciences, vol. 92, no. 10, pp. 2090–2097, Oct. 2003.

[34] D. Farrakhova et al., "Fluorescence imaging analysis of distribution of indocyanine green in molecular and nanoform in tumor model," Photodiagnosis and Photodynamic Therapy, vol. 37, p. 102636, Mar. 2022, doi: 10.1016/j.pdpdt.2021.102636.

[35] E. Spartalis et al., "Intraoperative Indocyanine Green (ICG) Angiography for the Identification of the Parathyroid Glands: Current Evidence and Future Perspectives," In Vivo, vol. 34, no. 1, pp. 23–32, 2020, doi: 10.21873/invivo.11741.

[36] D. J. DeDora et al., "Sulfobutyl ether β-cyclodextrin and methyl β-cyclodextrin enhance and stabilize fluorescence of aqueous indocyanine green: Sulfobutyl Ether β-Cyclodextrin and METHYL β-Cyclodextrin," J. Biomed. Mater. Res., vol. 104, no. 7, pp. 1457–1464, Oct. 2016, doi: 10.1002/jbm.b.33496.

[37] R. Weigand, F. Rotermund, and A. Penzkofer, "Degree of aggregation of indocyanine green in aqueous solutions determined by Mie scattering," Chemical Physics, vol. 220, no. 3, pp. 373–384, Aug. 1997, doi: 10.1016/S0301-0104(97)00150-X.

[38] P. C. Hiemenz and R. D. Vold, "Particle size from the optical properties of flocculating carbon dispersions," Journal of Colloid and Interface Science, vol. 21, no. 5, pp. 479–488, May 1966, doi: 10.1016/0095-8522(66)90046-8.

[39] NKT Photonics, "HC-800-02 Hollow Core Photonic Bandgap Fiber," HC-800-02.

[40] NKT Photonics, "HC-1550-02 Hollow Core Photonic Bandgap Fiber," HC-1550-02.

[41] A. J. Cox, A. J. DeWeerd, and J. Linden, "An experiment to measure Mie and Rayleigh total scattering cross sections," American Journal of Physics, vol. 70, no. 6, pp. 620–625, Jun. 2002, doi: 10.1119/1.1466815.

[42] D. V. Vezenov, B. T. Mayers, D. B. Wolfe, and G. M. Whitesides, "Integrated fluorescent light source for optofluidic applications," Appl. Phys. Lett., vol. 86, no. 4, p. 041104, Jan. 2005, doi: 10.1063/1.1850610.

[43] C. L. Bliss, J. N. McMullin, and C. J. Backhouse, "Integrated wavelength-selective optical waveguides for microfluidic-based laser-induced fluorescence detection," Lab Chip, vol. 8, no. 1, pp. 143–151, 2008, doi: 10.1039/B711601B.

[44] R. S. Conroy, B. T. Mayers, D. V. Vezenov, D. B. Wolfe, M. G. Prentiss, and G. M. Whitesides, "Optical waveguiding in suspensions of dielectric particles," p. 5.

[45] A. A. Boghossian et al., "Near-Infrared Fluorescent Sensors based on Single-Walled Carbon Nanotubes for Life Sciences Applications," ChemSusChem, vol. 4, no. 7, pp. 848–863, Jul. 2011, doi: 10.1002/cssc.201100070.

[46] D. A. Heller et al., "Multimodal optical sensing and analyte specificity using single-walled carbon nanotubes," Nature Nanotech, vol. 4, no. 2, pp. 114–120, Feb. 2009, doi: 10.1038/nnano.2008.369.

[47] X. He et al., "Carbon nanotubes as emerging quantum-light sources," Nature Mater, vol. 17, no. 8, pp. 663–670, Aug. 2018, doi: 10.1038/s41563-018-0109-2.

[48] S. Maruyama, Nanotube coordinate generator with a viewer for Windows [Online]. Available: http://www.photon.t.u-tokyo.ac.jp/ maruyama/wrapping3/wrapping.html

[49] A. Cusano et al., "Optical probes based on optical fibers and single-walled carbon nanotubes for hydrogen detection at cryogenic temperatures," Appl. Phys. Lett., vol. 89, no. 20, p. 201106, Nov. 2006, doi: 10.1063/1.2370292.

[50] S. Dresselhaus, "PHYSICS OF CARBON NANOTUBES," Carbon, 33(7), 883-891, 1995.

[51] V. Popov, "Carbon nanotubes: properties and application," Materials Science and Engineering: R: Reports, vol. 43, no. 3, pp. 61–102, Jan. 2004.

[52] S. Yamashita, "Nonlinear optics in carbon nanotube, graphene, and related 2D materials," APL Photonics, vol. 4, no. 3, p. 034301, Mar. 2019.

[53] R. Saito, M. Fujita, G. Dresselhaus, and M. S. Dresselhaus, "Electronic structure of chiral graphene tubules," Appl. Phys. Lett., vol. 60, no. 18, pp. 2204–2206, May 1992.

[54] C. Thomsen, S. Reich, and J. Maultzsch, Carbon Nanotubes: Basic Concepts and Physical Properties, 1st ed. Wiley, 2004.

[55] H. Kataura et al., "Optical properties of single-wall carbon nanotubes," Synthetic Metals, vol. 103, no. 1–3, pp. 2555–2558, Jun. 1999.

[56] R. Saito, G. Dresselhaus, and M. S. Dresselhaus, "Trigonal warping effect of carbon nanotubes," Phys. Rev. B, vol. 61, no. 4, pp. 2981–2990, Jan. 2000, doi: 10.1103/PhysRevB.61.2981.

[57] S. Maruyama, Fullerene and Carbon Nanotube Site [Online]. Available: http://www.photon.t.u-tokyo.ac.jp/ maruyama/nanotube.html

[58] S. Yamashita, "A Tutorial on Nonlinear Photonic Applications of Carbon Nanotube and Graphene," J. Lightwave Technol., vol. 30, no. 4, pp. 427–447, Feb. 2012.

[59] A. Gambetta et al., "Sub-100 fs two-color pump-probe spectroscopy of Single Wall Carbon Nanotubes with a 100 MHz Er-fiber laser system," p. 8, 2008.

[60] R. B. Weisman and S. M. Bachilo, "Dependence of Optical Transition Energies on Structure for Single-Walled Carbon Nanotubes in Aqueous Suspension: An Empirical Kataura Plot," Nano Lett., vol. 3, no. 9, pp. 1235–1238, Sep. 2003.

[61] S. M. Bachilo, M. S. Strano, C. Kittrell, R. H. Hauge, R. E. Smalley, and R. B. Weisman, "Structure-Assigned Optical Spectra of Single-Walled Carbon Nanotubes," Science, vol. 298, no. 5602, pp. 2361–2366, Dec. 2002.

[62] S. Giordani et al., "Debundling of Single-Walled Nanotubes by Dilution: Observation of Large Populations of Individual Nanotubes in Amide Solvent Dispersions," J. Phys. Chem. B, vol. 110, no. 32, pp. 15708–15718, Aug. 2006.

[63] A. Martinez and S. Yamashita, "Carbon Nanotube-Based Photonic Devices: Applications in Nonlinear Optics," In: J. M. Marulanda, Ed., Carbon Nanotubes Applications on Electron Devices, InTech, 2011.

[64] Vl. A. Margulis and T. A. Sizikova, "Theoretical study of third-order nonlinear optical response of semiconductor carbon nanotubes," Physica B: Condensed Matter, vol. 245, no. 2, pp. 173–189, Mar.1998.

[65] E. Turek, T. Shiraki, T. Shiraishi, T. Shiga, T. Fujigaya, and D. Janas, "Single-step isolation of carbon nanotubes with narrow-band light emission characteristics," Sci Rep, vol. 9, no. 1, p. 535, Dec. 2019

[66] M. Chernysheva et al., "Carbon nanotubes for ultrafast fibre lasers," Nanophotonics, vol. 6, no. 1, pp. 1–30, Jan. 2017, doi: 10.1515/nanoph-2015-0156.

[67] C. S. Goh et al., "Femtosecond mode-locking of a ytterbium-doped fiber laser using a carbon-nanotube-based mode-locker with ultra-wide absorption band," in (CLEO). Conference on Lasers and Electro-Optics, 2005., Baltimore, MD, USA, 2005, pp. 1644-1646 Vol. 3. doi: 10.1109/CLEO.2005.202227.

[68] K. Kieu and F. W. Wise, "All-fiber normal-dispersion femtosecond laser," Opt. Express, vol. 16, no. 15, p. 11453, Jul. 2008, doi: 10.1364/OE.16.011453.

[69] Y. Z. Pan, J. G. Miao, W. J. Liu, X. J. Huang, and Y. B. Wang, "Mode-locked ytterbium fiber lasers using a large modulation depth carbon nanotube saturable absorber without an additional spectral filter," Laser Phys. Lett., vol. 11, no. 9, p. 095105, Sep. 2014, doi: 10.1088/1612-2011/11/9/095105.

[70] NKT Photonics, "2 μm Range Hollow Core Photonic Bandgap Fiber,"HC-2000-01.

[71] NKT Photonics, "Hollow Core Photonic Bandgap Fiber for 1060nm Range Applications,"HC-1060-02.

[72] A. Hendler-Neumark and G. Bisker, "Fluorescent Single-Walled Carbon Nanotubes for Protein Detection," Sensors, vol. 19, no. 24, p. 5403, Dec. 2019, doi: 10.3390/s19245403.

[73] X. Wei et al., "Photoluminescence Quantum Yield of Single-Wall Carbon Nanotubes Corrected for the Photon Reabsorption Effect," p. 23.

[74] F. Schöppler et al., "Molar Extinction Coefficient of Single-Wall Carbon Nanotubes," J. Phys. Chem. C, vol. 115, no. 30, pp. 14682–14686, Aug. 2011, doi: 10.1021/jp205289h.

[75] A. J. Blanch, C. E. Lenehan, and J. S. Quinton, "Parametric analysis of sonication and centrifugation variables for dispersion of single walled carbon nanotubes in aqueous solutions of sodium dodecylbenzene sulfonate," Carbon, vol. 49, no. 15, pp. 5213–5228, Dec. 2011, doi: 10.1016/j.carbon.2011.07.039.

[76] A. Ansón-Casaos, J. M. González-Domínguez, I. Lafragüeta, J. A. Carrodeguas, and M. T. Martínez, "Optical absorption response of chemically modified single-walled carbon nanotubes upon ultracentrifugation in various dispersants," Carbon, vol. 66, pp. 105–118, Jan. 2014, doi: 10.1016/j.carbon.2013.08.048.

[77] S. H. Jeong, K. K. Kim, S. J. Jeong, K. H. An, S. H. Lee, and Y. H. Lee, "Optical absorption spectroscopy for determining carbon nanotube concentration in solution," Synthetic Metals, vol. 157, no. 13–15, pp. 570–574, Jul. 2007, doi: 10.1016/j.synthmet.2007.06.012.

[78] D. A. Tsyboulski, J.-D. R. Rocha, S. M. Bachilo, L. Cognet, and R. B. Weisman, "Structure-Dependent Fluorescence Efficiencies of Individual Single-Walled Carbon Nanotubes," Nano Lett., vol. 7, no. 10, pp. 3080–3085, Oct. 2007, doi: 10.1021/nl071561s.

[79] K. Ding et al., "Research on Narrow Linewidth External Cavity Semiconductor Lasers," Crystals, vol. 12, no. 7, p. 956, Jul. 2022, doi: 10.3390/cryst12070956.

[80] F. J. Duarte, Ed., Organic Lasers and Organic Photonics, Bristol, IOP, 2018. doi: 10.1007/978-3-662-11579-4.

[81] F. P. Schäfer, Ed., Dye Lasers, vol. 1. Berlin, Heidelberg: Springer Berlin Heidelberg, 1973. doi: 10.1007/978-3-662-11579-4.

[82] B. Pierce and R. Birge, "Lasing properties of several near-IR dyes for a nitrogen laser-pumped dye laser with an optical amplifier," IEEE J. Quantum Electron., vol. 18, no. 7, pp. 1164–1170, Jul. 1982, doi: 10.1109/JQE.1982.1071672.

[83] Robert A. Norwood, "Organic Photonics: Ready for Prime Time," Optics & Photonics News 24(11), 40-47, 2013.

[84] M. Stuke, Dye Lasers: 25 Years. Berlin, Heidelberg: Springer-Verlag Springer, ch.11, 2005.

APPENDICES

Appendix A

Radii Estimates for ICG Aggregates in HCPBF

For aggregating nanoparticles, the size of the aggregates may be significant in optical density calculations within HCPBF. Here we calculate the potential range of ICG radii from the data presented in Chapter 4. While the experimental and calculated number density for particles within the fiber seem to agree, this study only takes into account scattering effects which may no be applicable to fluorescing particles. However, this assumption would certainly be valid when considering dielectric particles dispersed in liquid fibers.

For ICG dispersed in water, molecule aggregate radii have been measured between $2nm - 200nm$ [36], with J-aggregates forming at radii $> 50nm$[37]. Due to the low concentration samples of dye used in out experiments, the lower range of molecule diameter is expected, meeting the Raleigh scattering approximation condition $\frac{2\pi r}{\lambda} << 1$, the scattering cross-section is

$$\sigma_0 = \frac{2\pi^5 (2r_{particle})^6}{3\lambda^4} (\frac{N^2 - 1}{N^2 + 2})^2 \tag{A.1}$$

where $N = \frac{n_{particle}}{n_{solvent}}$. After applying the parameters above and (A.1) to (3.31), the estimated concentration of ICG molecules for optically dense medium ($OD_{fiber} = 1$) has a range of $N_{particle} = 1.5 \times 10^8 \sim 2.0 \times 10^{14}$ molecules and $N_{particle} = 8.2 \times 10^7 \sim 1.1 \times 10^{14}$ molecules for 1550nm and 800nm HCPBF respectively varying the ICG aggregate radii within the approximation condition.

For calculations of optical density with ICG molecules in the 1550nm HCPBF, the core radius is taken as $r_{core} = 5 \pm 0.05\mu m$ with beam waist $w_0 = 4.5 \pm 0.05\mu m$. For this $L_{fiber} = 1cm$ piece of fiber, the number of molecules contained in a perfectly filled core is

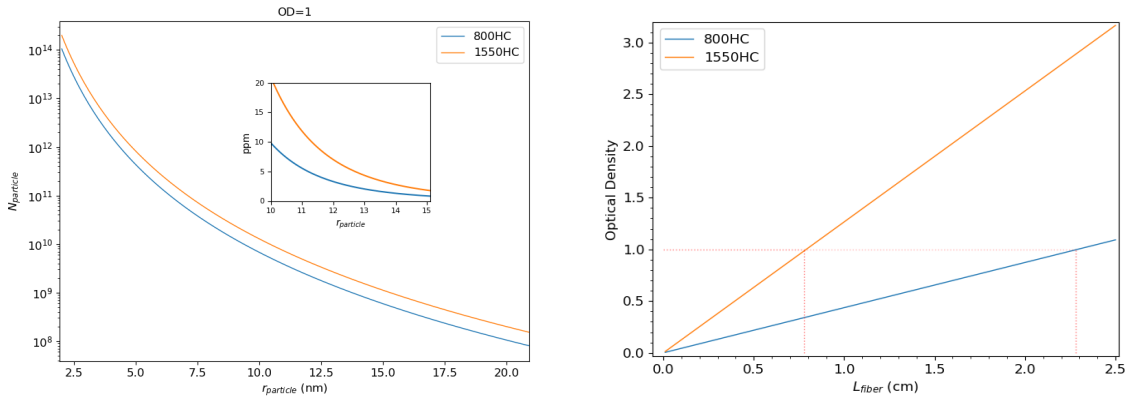

(a) (b)

Figure A.1: (a)The number of molecules to create an optically dense medium as a function of average particle radius. Inset plot shows the dye concentration as a function of particle radius.(b) The rate increase in OD as the length of the fiber increases. For $OD = 1$: a sample concentration of 3.7ppm in 80nm HCPBF, $L_{fiber} = 2.28cm$ with a rate of $0.44(\frac{OD}{cm})$. For 1550nm HCPBF with a sample concentration of 4ppm. $L_{fiber} = 0.78cm$ with a rate of $1.27(\frac{OD}{cm})$

expected to be

$$N_{particle} = M_{ICG} * C * V_{fiber} = \frac{1mol}{774.98g} * \frac{4mg}{1dm^3} * \pi(5\mu m)^2(1cm) = 2.441 \times 10^9 molecules \tag{A.2}$$

Using the measured optical density in the fiber, Fig.5.7b the estimated radius of the aggregate ICG molecules is $r_{particle} = 13.7 \pm 0.2$nm. Carrying out the same calculations for the $L_{fiber} = 2cm$ 800nm HCPBF, the number of molecules contained in a perfectly filled core will be $N_{particle} = 2.54 \times 10^9$. The fiber has a core radius $r_{core} = 3.75 \pm 0.05\mu m$ with beam waist $w_0 = 2.75 \pm 0.05$ and using the measured optical density in the fiber, Fig.5.8a, the estimated radius of the aggregate ICG molecules is $r_{particle} = 11.5 \pm 0.26$nm. These molecule radii are well in agreement, but since the 800nm HCPBF ICG solution is a slightly lower concentration, the average $r_{particle}$ is expected to form slightly smaller aggregates.